RSC
Applied Interfaces

PAPER

View Article Online
View Journal

Open Access Article. Published on 27 May 2026. Downloaded on 6/18/2026 4:45:20 AM.
This article is licensed under a Creative Commons Attribution 3.0 Unported Licence.

Check for updates

Cite this: DOI: 10.1039/d6lf00078a

Received 9th March 2026,
Accepted 22nd May 2026

DOI: 10.1039/d6lf00078a

rsc.li/RSCApplInter

Nanoclay-enhanced self-healing of polyurethane–urea coatings enabled by disulfide exchange

Ronak Ansaripour, † Maryam Bonyani † and Sitaraman Krishnan *

Functional materials that combine mechanical robustness with autonomous self-healing are highly desirable for coatings and structural materials operating in aqueous environments. Here we report amphiphilic polyurethane–urea (PUU) networks incorporating polyethylene glycol (PEG) and polydimethylsiloxane (PDMS) segments together with dynamic urea linkages and aromatic disulfide bonds introduced *via* 4,4′-diaminodiphenyl disulfide (DPDS), further reinforced with amine-functionalized montmorillonite nanoclay. Density functional theory calculations establish the energetic hierarchy of the relevant dynamic bond reactions in vacuum and water, indicating that urea-related and disulfide pathways are kinetically accessible under moderate conditions, whereas urethane exchange is substantially less favorable. Guided by these insights, PUU networks and nanoclay composites were synthesized and characterized structurally and mechanically. The nanoclay was well dispersed within the amphiphilic matrix and significantly increased the storage modulus of the materials. Remarkably, incorporation of amine-functionalized nanoclay accelerated healing kinetics despite substantially increasing the modulus of the network, mitigating the conventional trade-off between stiffness and self-healing. Tensile healing experiments showed that nanoclay-reinforced PUU-DPDS networks achieved nearly complete mechanical recovery, with toughness reaching 94% in air and 81% under water after 24 h. At elevated temperature, the strength recovered to about 90% after 8 h at 60 °C. These results demonstrate that reactive nanoclay nanoparticles can simultaneously reinforce polyurethane–urea networks and promote dynamic bond exchange, enabling mechanically robust coatings with efficient self-repair in both dry and aqueous environments.

1 Introduction

Polyurethane (PU) thermoplastics and thermosets are widely used in automotive, aerospace, marine, and biomedical applications due to their tunable mechanical properties, which arise from a microphase-separated architecture of alternating soft and hard segments. Soft segments derived from long-chain polyols confer flexibility, while hard segments formed from diisocyanates and multifunctional crosslinkers impart strength and rigidity, enabling a balance of elasticity and toughness.[1,2] However, the growing use of PUs in long-term structural applications has raised concerns about sustainability, limited repairability, and the accumulation of persistent plastic waste.[3] To address these challenges, recent efforts have focused on developing durable, reprocessable materials that align with circular economy principles.[4] One promising approach is the incorporation of dynamic covalent bonds into PU networks, which enables both recyclability and self-healing functionality.[5] These dynamic bonds allow the material to restore mechanical integrity after damage, either autonomously or in response to external stimuli, thereby extending service life and reducing environmental impact.[6]

Dynamic covalent bonding in polyurethane-based materials

Dynamic covalent chemistry has emerged as an effective strategy for engineering adaptable polymer networks capable of rearranging their crosslinked structures in response to external stimuli.[7] Such covalent adaptable networks enable network reconfiguration through reversible bond exchange while maintaining the overall crosslink density, thereby enabling properties such as healing, recyclability, and stress relaxation.[8] In PU-based materials, these concepts have been implemented through a variety of dynamic covalent mechanisms that allow network rearrangement without permanent degradation of the crosslinked architecture.[9] As a result, the material can undergo structural reorganization while largely preserving its modulus and mechanical strength.

Department of Chemical & Biomolecular Engineering, Clarkson University, 8 Clarkson Avenue, Potsdam, New York, USA. E-mail: skrishna@clarkson.edu; Tel: +1 315 268 6661

† These authors contributed equally to this work.

© 2026 The Author(s). Published by the Royal Society of Chemistry

Open Access Article. Published on 27 May 2026. Downloaded on 6/18/2026 4:45:20 AM.
This article is licensed under a Creative Commons Attribution 3.0 Unported Licence.

Several dynamic covalent mechanisms have been reported in PU systems, including aromatic disulfide exchange,[10,11] urea exchange,[12,13] urethane exchange in catalyst-assisted vitrimer networks,[14] imine metathesis,[15] and boron-based dynamic bonds.[16] Diels–Alder reactions likewise belong to this class of thermally reversible covalent chemistries, although they often require elevated temperatures to trigger bond dissociation and reformation.[17] Compared with noncovalent interactions such as hydrogen bonding,[18] van der Waals interactions,[19,20] or metal–ligand coordination, which often provide rapid but mechanically weaker and environmentally sensitive reversibility, dynamic covalent networks combine mechanical robustness with adaptive functionality.[21,22] This balance makes them particularly attractive for polyurethane materials requiring durability, repairability, and sustainability, providing a versatile molecular foundation for intrinsic self-healing and circular material design.

Balancing chain diffusion and bond exchange for effective healing

In the work reported here, we focus specifically on the role of dynamic covalent bonds in the self-healing of PU coatings, particularly under aqueous conditions. Effective healing at damaged interfaces depends on the interplay between chain diffusion and dynamic bond exchange.[23] The diffusion coefficient, which governs chain mobility, is determined by molecular weight and segmental mobility, this latter being directly linked to the glass transition temperature (T_g). Below T_g, limited mobility restricts diffusion regardless of bond exchange kinetics, while slow bond exchange can limit healing even when diffusion is adequate. Thus, balanced chain mobility and bond exchange rates are essential. Otherwise, healing becomes diffusion- or kinetics-limited, resulting in incomplete recovery.[24]

Underwater, achieving a balance between chain diffusion and dynamic bond exchange remains challenging in self-healing polymer systems. Water, as a polar protic solvent with high cohesive energy density and an extensive hydrogen-bonding network, can influence reaction environments through hydrogen-bonding and solvation effects that modify transition states and reaction pathways.[25,26] In polymer networks, absorbed water may plasticize the material, lowering the effective T_g and increasing segmental mobility, thereby facilitating chain diffusion across damaged interfaces.[27–29] Conversely, water can compete with polymer–polymer interactions, perturb intermolecular forces and chain packing, or hydrolyze water-sensitive dynamic covalent bonds, thereby reducing healing efficiency.[28,30] These competing effects complicate the prediction of underwater self-healing behavior and highlight the need for experimental validation and molecular-level understanding to guide the design of PU coatings for aquatic environments.

Literature studies on water-compatible dynamic bond systems

Recent advances in self-healing PU coatings have increasingly focused on dynamic covalent chemistries capable of operating in aqueous environments. Nevertheless, many reversible linkages remain inherently susceptible to hydrolytic degradation, limiting long-term underwater durability. Huang *et al.*[29] addressed this challenge by designing a PU derived from hydroxy-terminated polybutadiene (HTPB) that incorporates water-sensitive dynamic imine bonds together with aliphatic long-chain glycerol monostearate. The hydrophobic HTPB backbone, together with the long alkyl side chains introduced by glycerol monostearate, forms a protective barrier that restricts excessive water ingress while maintaining sufficient segmental mobility to activate imine metathesis. As a result, the material retained 81% of its tensile strength after 3 days of immersion and achieved self-healing efficiencies of 95% at 35 °C in air and 79% underwater.

Mechanistic analysis revealed that limited water uptake can assist imine hydrolysis–reformation cycles, whereas excessive water absorption disrupts hydrogen-bonded networks and compromises structural stability. Thus, the study highlights a critical design principle for underwater PU systems: dynamic bond activation requires controlled water permeability, yet excessive hydrophilicity accelerates bond degradation and mechanical decay. Achieving this balance between hydrophobic shielding and molecular mobility is central to the development of robust, water-tolerant self-healing coatings.

To address the hydrolytic instability of imine-based systems, Li *et al.*[31] incorporated disulfide and imine linkages into a hydrophobic polyurethane framework. This design enabled the material to recover up to 98% of its original tensile strength after 12 h of healing under water. The system also incorporated dual hydrophobic domains, alkyl side chains and fluorinated segments, that shield the dynamic bonds from water interference and preserve network integrity during immersion. Small-molecule exchange experiments confirmed cooperative disulfide–imine bond dynamics that facilitate network rearrangement. These results highlight that effective underwater self-healing depends not only on reversible covalent chemistry but also on dynamic motifs capable of sustaining bond exchange while resisting hydrolytic disruption.

Waterborne polyurethane (WPU) systems further highlight the importance of chemically stable dynamic cross-links. Zhang *et al.*[16] incorporated borate ester linkages stabilized by boron–nitrogen internal coordination into WPU coatings, achieving 83% healing efficiency together with enhanced tensile strength (24.2 MPa) and improved water resistance after 24 h of immersion. The intramolecular coordination suppresses hydrolysis of the borate esters, illustrating how molecular-level stabilization can shift the dynamic equilibrium toward greater durability under aqueous conditions. These findings broaden the design space for dynamic bonds beyond inherently labile chemistries, suggesting that even relatively stable covalent linkages can be rendered reversible under suitable catalytic or structural conditions.

© 2026 The Author(s). Published by the Royal Society of Chemistry

Open Access Article. Published on 27 May 2026. Downloaded on 6/18/2026 4:45:20 AM. This article is licensed under a Creative Commons Attribution 3.0 Unported Licence.

While dynamic bond selection governs healing kinetics, mechanical robustness remains equally critical for coating durability. Nanofiller reinforcement is widely employed to enhance modulus and toughness. However, conventional fillers often restrict segmental mobility and elevate T_g, which can limit healing efficiency. For example, incorporation of polydopamine-modified halloysite nanotubes increased the Young's modulus to ≈101 MPa and the tensile strength to ≈68 MPa through strong interfacial hydrogen bonding, but also raised the glass transition temperature, thereby limiting chain mobility and preventing improvement in healing efficiency.[32] In contrast, two-dimensional nanoclay platelets can significantly influence fracture mechanics rather than merely stiffening the matrix. In our previous work, surface-functionalized nanoclay produced ≈6× higher tear resistance, ≈4× higher rubbery plateau modulus, and ≈2× higher toughness than carbon black at equivalent loading.[33] The >500% increase in tear resistance was attributed to synergistic crack deflection and polymer–filler co-network formation, which enhance interfacial stress transfer and viscous energy dissipation ahead of the crack tip. These observations highlight the ability of reactive, two-dimensional nanoclay platelets to influence interfacial mechanics beyond conventional filler reinforcement.

Recent studies have also explored strategies to reconcile high mechanical strength with efficient self-healing in polyurethane elastomers through molecular-level reinforcement. For example, Huang *et al.*[34] reported a polyurethane elastomer incorporating rigid poly(amic acid) (PAA) chain segments together with a chain extender containing sextuple hydrogen-bonding units and aliphatic disulfide bonds derived from 3,3-dithiodipropionic dihydrazide. The rigid PAA domains enhance intermolecular interactions and chain packing, enabling tensile strengths up to 50.1 MPa. Dynamic disulfide exchange provides the covalent mechanism for network rearrangement, while the dense hydrogen-bonding arrays facilitate reversible intermolecular association and energy dissipation. As a result, the elastomer achieves a self-healing efficiency of 96% after 12 h of thermal activation at 80 °C. These results demonstrate that rigid segment reinforcement combined with reversible covalent exchange can produce mechanically robust self-healing polyurethane networks. However, healing in such systems relies on elevated temperatures to activate network rearrangement, and their behavior has been examined primarily under dry conditions.

Despite substantial progress, a quantitative energetic comparison of dynamic linkages under submerged conditions remains lacking. In particular, the relative kinetic accessibility and thermodynamic stability of urea, urethane, and aromatic disulfide exchange in aqueous environments have not been systematically established. Because water can modify activation barriers, solvation energies, and bond dissociation equilibria, defining this mechanistic hierarchy is essential for rational molecular design. Establishing such a comparative energetic framework enables predictive selection of dynamic motifs capable of sustaining autonomous healing under continuous water immersion while preserving mechanical integrity.

Knowledge gaps in underwater PU systems

Building on these insights, this study examined polyurethane nanocomposites designed to exhibit autonomous self-healing under continuous water immersion without external stimuli. While many existing systems demonstrate self-repair in dry environments or require external triggers such as heat or light, few reliably heal under fully submerged conditions, an essential capability for marine coatings, long-term fluid-exposed biomedical coatings, and structurally inaccessible submerged systems.[27]

Based on these considerations, we designed an amphiphilic polyurethane–urea (PUU) elastomer incorporating hydrophilic polyethylene glycol (PEG) and hydrophobic polydimethylsiloxane (PDMS) segments. This dual-segment architecture balances controlled water uptake with matrix stability, providing sufficient chain mobility for bond exchange while preventing excessive plasticization during prolonged immersion. Aromatic disulfide and urea linkages were introduced to enable autonomous, room-temperature dynamic exchange.

Mechanical durability was further improved without sacrificing network dynamicity by incorporating amine-functionalized montmorillonite nanoclay. Owing to its two-dimensional platelet morphology and interfacial reactivity,[33] layered nanoclay was initially introduced to reinforce the network while mitigating the conventional trade-off between stiffness and healing efficiency. Unlike previously reported one-dimensional fillers such as halloysite nanotubes,[32] two-dimensional clay platelets create extended polymer–filler interfaces that fundamentally alter fracture processes. Consistent with observations from our earlier work,[33] AMMT incorporation significantly enhanced mechanical robustness while unexpectedly increasing the healing rate under immersion. This finding suggests that layered nanoclays can actively influence crack-tip dynamics and interfacial bond exchange processes rather than merely acting as passive mechanical reinforcements.

To clarify the intrinsic factors governing underwater healing, we first established a molecular-level energetic hierarchy of urea, urethane, and aromatic disulfide exchange using density functional theory (DFT) in both vacuum and with aqueous solvation effects. These calculations provided a thermodynamic and kinetic basis for comparing dynamic bond accessibility under immersion. The computational insights were subsequently evaluated through synthesis, structural characterization, and underwater healing experiments. Together, this approach links intrinsic bond energetics to macroscopic healing performance, while the role of nanoclay was assessed

Open Access Article. Published on 27 May 2026. Downloaded on 6/18/2026 4:45:20 AM.
This article is licensed under a Creative Commons Attribution 3.0 Unported Licence.

experimentally through its influence on mechanical integrity and healing kinetics.

Experimental and theoretical methodology

DFT calculations were performed to quantify the thermodynamic and kinetic characteristics of urea, urethane, and aromatic disulfide exchange reactions in both vacuum and with aqueous solvation effects using the SMD (solvation model based on density)[35] continuum solvation model. Full Gibbs free energy profiles were constructed, and activation free energies, overall reaction free energies, and rate-determining barriers were extracted. Intrinsic reaction coordinate (IRC) analyses[36] confirmed connectivity between stationary points and distinguished concerted from stepwise mechanisms, providing a quantitative energetic hierarchy of bond dynamicity under submerged conditions.

Guided by these molecular insights, amphiphilic PUU elastomers and nanoclay-reinforced composites were synthesized and systematically characterized. Nanoclay dispersion and structural organization were evaluated using X-ray diffraction (XRD). Thermophysical behavior and segmental mobility were examined by differential scanning calorimetry (DSC) and dynamic mechanical analysis (DMA). Surface energy and amphiphilicity were assessed using contact angle measurements and Owens–Wendt analysis. Mechanical recovery experiments in air and under continuous water immersion were then conducted to evaluate healing kinetics and experimentally validate the bond-exchange mechanisms predicted by DFT. Together, this combined theoretical and experimental approach establishes a direct link between molecular energetics, network structure, and macroscopic self-healing behavior.

2 Results and discussion

2.1 DFT analysis of urea, urethane, and disulfide reaction mechanisms

Simplified molecular models were constructed to represent the local reactive motifs governing bond reactivity. Because explicit modeling of full polymer chains is computationally prohibitive at the DFT level, truncated compounds were employed that retain the essential reactive groups. Diethyl urea and diethyl urethane were used as representative systems, with larger polymer substituents replaced by ethyl groups, while disulfide exchange was modeled using diphenyl disulfide (Ph–S–S–Ph), representing the aryl disulfide units present in the polymer network. Consistent with prior studies,[13] these models are intended to capture the elementary bond-breaking and bond-forming steps relevant to exchange processes. This approach preserves the local chemical environment of the reactive bonds while maintaining computational tractability.

This reduced-model approach isolates the intrinsic electronic factors governing bond reactivity and is widely used in DFT studies of dynamic polymer networks, where small-molecule analogues capture the primary features of bond-breaking and bond-forming processes, while steric, solvation, and network effects modulate the effective activation barriers.[7,12]

The simplified molecular models do not capture polymer-specific effects such as restricted segmental mobility, intermolecular packing, and cooperative hydrogen bonding, which influence activation barriers and accessibility of reactive sites. Therefore, the computed activation free energies represent intrinsic reactivity trends rather than quantitative condensed-phase kinetics.

Macroscopic exchange kinetics, however, depend on network-level parameters such as crosslink density, topology, and chain mobility.[37] The present calculations therefore provide a basis for comparing intrinsic reactivity across chemistries, while experimentally observed variations reflect these higher-order constraints. Trends in activation energetics from small-molecule models can provide useful qualitative guidance for bond exchange behavior in polymer networks.[13]

To compare the intrinsic energetic trends governing representative dynamic covalent reactions, Gibbs free energy profiles were computed for urea, urethane, and aromatic disulfide reactions in both vacuum and under aqueous solvation (SMD) using a consistent DFT protocol. Intrinsic reaction coordinate (IRC) calculations were performed to confirm connectivity between stationary points and to distinguish concerted from stepwise pathways.

For each system, the Gibbs free energy of activation, $\Delta G^{\ddagger}$, was defined as

$$\Delta G^{\ddagger} = G_{\mathrm{TS}} - G_{\mathrm{ref}} \tag{1}$$

where G_{TS} and G_{ref} denote the Gibbs free energies of the transition state and the preceding minimum (reactant or intermediate), respectively. The rate-determining activation free energy, $\Delta G^{\ddagger}_{\mathrm{RDS}}$, was taken as the largest $\Delta G^{\ddagger}$ along the reaction pathway. The overall reaction free energy was defined as

$$\Delta G_{\mathrm{rxn}} = G_{\mathrm{products}} - G_{\mathrm{reactants}} \tag{2}$$

The relationship between activation free energy and reaction rate is given by transition state theory:

$$k = \frac{k_{\mathrm{B}}T}{h}\exp\left(\frac{-\Delta G^{\ddagger}}{RT}\right) \tag{3}$$

highlighting the exponential dependence of the rate constant on $\Delta G^{\ddagger}$. Accordingly, the magnitude of $\Delta G^{\ddagger}_{\mathrm{RDS}}$ was used as a measure of kinetic accessibility.

The computed free energy profiles (Fig. 1) and corresponding activation barriers and reaction free energies (Tables 1 and 2) reveal distinct, chemistry-dependent solvent effects.

Urea reaction. In vacuum (Fig. 1a), the urea reaction proceeds through a single transition state with $\Delta G^{\ddagger}_{\mathrm{RDS}} = 14.8$

Open Access Article. Published on 27 May 2026. Downloaded on 6/18/2026 4:45:20 AM.
This article is licensed under a Creative Commons Attribution 3.0 Unported Licence.

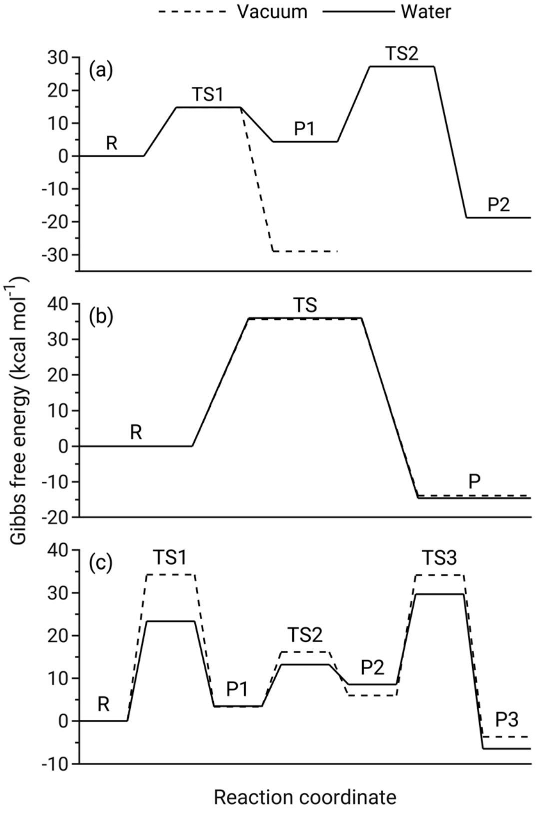

Fig. 1 Computed Gibbs free energy profiles for representative dynamic covalent reactions at the B3LYP/6-31+G(d,p) level of theory (25 °C, 1 atm). (a) Urea formation (ethyl isocyanate/amine); (b) urethane formation (ethyl isocyanate/alcohol); (c) disulfide exchange (diphenyl disulfide). Dashed lines denote vacuum; solid lines denote water (SMD). Energies were referenced to the reactant state.

Table 1 Rate-determining activation free energies ($\Delta G^{\ddagger}_{\mathrm{RDS}}$) and overall reaction free energies (ΔG_{rxn}) in kcal mol^{-1}

System	Medium	$\Delta G^{\ddagger}_{\mathrm{RDS}}$	ΔG_{rxn}	Pathway
Urea	Vacuum	14.8	−28.9	Single-step
Urea	Water	22.8	−18.8	Two-step
Urethane	Vacuum	35.6	−13.9	Single-step
Urethane	Water	36.0	−14.6	Single-step
Disulfide	Vacuum	34.3	−3.6	Three-step
Disulfide	Water	23.4	−6.4	Three-step

Table 2 Energetic span analysis for disulfide exchange (ΔG_{span}, kcal mol^{-1})

System	Vacuum	Water
ΔG_{span}	34.3	29.7

kcal mol^{-1} and an exergonic reaction free energy of $\Delta G_{\mathrm{rxn}} = -28.9$ kcal mol^{-1}. In water, the potential energy surface reorganizes into a stepwise mechanism featuring a stabilized intermediate. The highest elementary barrier increases to $\Delta G^{\ddagger}_{\mathrm{RDS}} = 22.8$ kcal mol^{-1}, while the reaction free energy decreases in magnitude to $\Delta G_{\mathrm{rxn}} = -18.8$ kcal mol^{-1}. Thus, solvation increases the kinetic barrier and alters the pathway topology from concerted to a two-step mechanism.

Because the aqueous pathway contains multiple stationary points, the energetic span was also evaluated. In water, $\Delta G_{\mathrm{span}} = 27.2$ kcal mol^{-1}, defined as the free energy difference between the reactant (TDI) and the second transition state (TDTS).

Urethane reaction. The urethane reaction (Fig. 1b) remains concerted in both environments and exhibits substantially higher activation free energies. In vacuum, $\Delta G^{\ddagger}_{\mathrm{RDS}} = 35.6$ kcal mol^{-1} with $\Delta G_{\mathrm{rxn}} = -13.9$ kcal mol^{-1}, while in water, $\Delta G^{\ddagger}_{\mathrm{RDS}} = 36.0$ kcal mol^{-1} and $\Delta G_{\mathrm{rxn}} = -14.6$ kcal mol^{-1}. The large barrier heights indicate intrinsically slow reaction kinetics under moderate thermal conditions.

Disulfide exchange. Disulfide exchange (Fig. 1c) proceeds through a three-step pathway in both media. In vacuum, $\Delta G^{\ddagger}_{\mathrm{RDS}} = 34.3$ kcal mol^{-1} and $\Delta G_{\mathrm{rxn}} = -3.6$ kcal mol^{-1}. In water, $\Delta G^{\ddagger}_{\mathrm{RDS}} = 23.4$ kcal mol^{-1} and $\Delta G_{\mathrm{rxn}} = -6.4$ kcal mol^{-1}. Unlike urea, solvation lowers the dominant elementary barrier for disulfide exchange.

Because disulfide exchange is multistep, the overall kinetic limitation was evaluated using the energetic span model of Kozuch and Shaik.[38,39] For the exergonic pathways considered here:

$$\Delta G_{\mathrm{span}} = G_{\mathrm{TDTS}} - G_{\mathrm{TDI}} \tag{4}$$

In vacuum, $\Delta G_{\mathrm{span}} = 34.3$ kcal mol^{-1} (TDI = reactant, TDTS = TS1). In water, $\Delta G_{\mathrm{span}} = 29.7$ kcal mol^{-1} (TDI = reactant, TDTS = TS3). For comparison, in water, the urea reaction is more exergonic than disulfide exchange (−18.8 *vs.* −6.4 kcal mol^{-1}) and exhibits a slightly smaller energetic span (27.2 *vs.* 29.7 kcal mol^{-1}).

Energetic hierarchy and implications. Comparison of $\Delta G^{\ddagger}_{\mathrm{RDS}}$ values (Table 1) establishes the kinetic ordering:

$$\text{Urea (water)} \approx \text{Disulfide (water)} \ll \text{Urethane}$$

At 298 K, a 10 kcal mol^{-1} difference corresponds to approximately seven to eight orders of magnitude change in the rate constant. Therefore, the 12–21 kcal mol^{-1} difference between urea/disulfide and urethane reactions implies substantially different dynamic timescales.

The urea pathway considered here corresponds to bond formation between amine and isocyanate species and thus provides insight into the intrinsic accessibility of urea formation relevant to exchange processes. The present DFT results establish the kinetic accessibility and solvent dependence of this pathway, but do not by themselves distinguish whether urea exchange in the polymer network proceeds predominantly through associative or dissociative mechanisms. This distinction is further complicated by sterically hindered urea linkages derived from IPDI, which are not explicitly represented in the simplified molecular model. In the literature, sterically hindered or activated urea systems are commonly described as exchanging predominantly through

Open Access Article. Published on 27 May 2026. Downloaded on 6/18/2026 4:45:20 AM. This article is licensed under a Creative Commons Attribution 3.0 Unported Licence.

Table 3 Comparison of rate-determining activation free energies ($\Delta G^{\ddagger}_{\text{RDS}}$) computed using B3LYP/6-31+G(d,p) and ωB97X-D/def2-TZVP (kcal mol^{-1})

System	Medium	B3LYP	ωB97X-D	Difference
Urea	Vacuum	14.8	12.6	−2.2
Urea	Water	22.8	21.2	−1.6
Urethane	Vacuum	35.6	33.0	−2.6
Urethane	Water	36.0	30.2	−5.8

dissociative pathways under appropriate conditions.[13,40,41] In contrast, the aromatic disulfide pathway considered here is stepwise, involving bond cleavage and recombination, and therefore exhibits mixed dissociative/associative character.[40] Despite these complexities, the present calculations establish comparative intrinsic reactivity trends and solvent-dependent behavior for urea, urethane, and disulfide linkages.

To assess the sensitivity of the activation barriers to the density functional, selected calculations were repeated using the range-separated ωB97X-D functional with the larger def2-TZVP basis set. The resulting $\Delta G^{\ddagger}_{\text{RDS}}$ values follow the same qualitative energetic hierarchy as the B3LYP/6-31+G(d,p) calculations (Table 3).

Table 4 Composition of PUU and PUU-DPDS formulations. Reactive components are reported in mmol, while processing components are reported in mass or volume as indicated. Approximate number-average molecular weights of precursor polymers: PEG ≈ 400 g mol^{-1}, PDMS ≈ 875 g mol^{-1}, and trifunctional amine crosslinker ≈ 440 g mol^{-1}

Component	PUU	PUU-DPDS
Monomers (mmol)		
α,ω-Dihydroxy PEG	0.67	0.65
α,ω-Diamino PDMS	1.01	1.00
4,4′-Diaminodiphenyl disulfide (APDS)	0.00	0.24
Trifunctional amine crosslinker	0.54	0.27
IPDI	2.37	2.36
Total mass, p (g)	1.917	1.840
Catalyst and solvent		
n-Butyltin dilaurate (μL)	1.5	1.5
Anhydrous THF (mL)	9.6	9.2

For the PUU-AMMT and PUU-DPDS-AMMT samples, a γ-APTES-functionalized MMT clay dispersion in THF (10 wt%) was added to achieve a target clay mass fraction $w = m_{\text{clay}}/(p + m_{\text{clay}})$, where p is the total polymer mass. The dispersion mass was calculated from its 10 wt% clay content ($m_{\text{disp}} = m_{\text{clay}}/0.10$), yielding final clay loadings of approximately $w \approx 3\%$ and 5%.

2.2 Synthesis of polyurethane–urea copolymers and films

PUU elastomers were synthesized according to the reaction scheme shown in Fig. 2 *via* a two-step solution polymerization process. In the first step, PEG was end-functionalized using isophorone diisocyanate (IPDI). In the second step, the resulting isocyanate-terminated PEG (**3**, Fig. 2) was reacted with amine-terminated PDMS (**4**) and other amine-functionalized components, namely 4,4′-diaminodiphenyl disulfide (APDS, **5**) and the trifunctional crosslinker trimethylolpropane tris[α-hydroxy-ω-amino-poly(propylene glycol)] ether (**6**).

The formulations were designed to achieve an approximately stoichiometric balance between nucleophilic

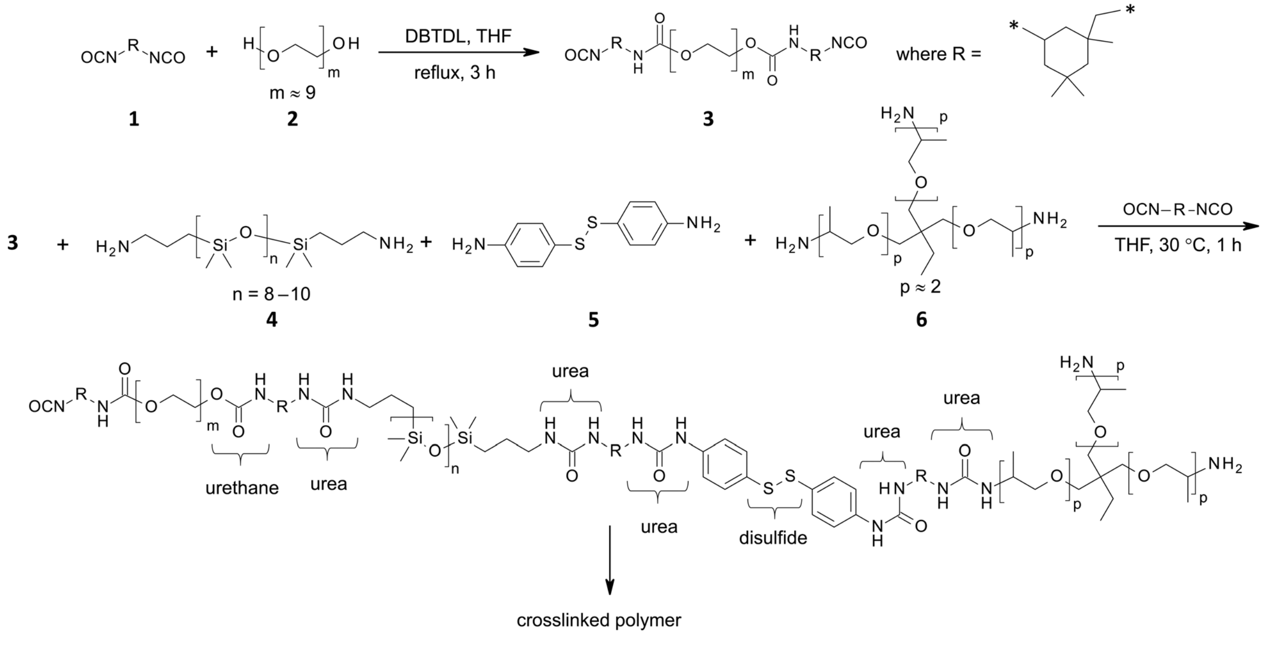

Fig. 2 Synthesis of the polyurethane–urea elastomer network incorporating PDMS soft segments and dynamic covalent bonds. Diisocyanate **1** reacts with PEG diol **2** in THF in the presence of DBTDL to form an isocyanate-terminated urethane prepolymer **3**. Subsequent reaction of **3** with α,ω-diamino PDMS **4**, 4,4′-diaminodiphenyl disulfide **5**, and a trifunctional polyether amine crosslinker **6** generates a polyurethane–urea network containing urethane linkages from the initial diol–isocyanate reaction and multiple urea linkages from amine–isocyanate reactions. The resulting polymer incorporates aromatic disulfide units and sterically hindered urea linkages derived from IPDI, which are capable of reversible bond exchange, and the multifunctional amine crosslinker establishes a three-dimensional crosslinked polymer network.

Open Access Article. Published on 27 May 2026. Downloaded on 6/18/2026 4:45:20 AM.
This article is licensed under a Creative Commons Attribution 3.0 Unported Licence.

(–OH, –NH_2) and isocyanate (–NCO) functionalities on the basis of functional-group equivalence (Table 4), with stoichiometric ratio factors close to unity. Under these conditions, gelation in an ideal step-growth system is expected only at high functional-group conversion, as predicted by Flory–Stockmayer theory (see SI). Consistent with this expectation, the reaction mixtures remained clear, viscous solutions (colorless for PUU and yellowish for PUU-DPDS) rather than forming macroscopic gels, indicating that the systems remained below the gel point during synthesis.

On this basis, the copolymer in solution is expected to consist of a distribution of linear and branched species arising from the incorporation of difunctional and trifunctional components. It is also plausible that a fraction of chains carried terminal isocyanate groups at this stage. These residual functionalities can react with available hydroxyl or amine groups during solvent removal and film formation, contributing to the development of the final network structure. Consistent with this, ATR-FTIR spectra of the cast films show no detectable isocyanate band (*vide infra*), indicating that residual –NCO, if present during synthesis, is not present at detectable levels in the final material.

Under the reaction conditions employed, limited secondary reactions of isocyanate groups, such as allophanate formation or reaction with trace residual moisture followed by urea formation, may occur and could contribute modestly to branching or effective crosslink density.

The compositions and processing parameters were optimized to yield non-sticky elastomeric films with sufficient toughness for handling and clean removal from the substrate without fracture. The disulfide content was experimentally tuned to balance elastomeric behavior with effective self-healing performance. Disulfide contents exceeding approximately 3 wt% 4,4′-diaminodiphenyl disulfide during copolymer synthesis led to vitrification and loss of elasticity. The final copolymer compositions used in this study are summarized in Table 4.

For the composite films, montmorillonite clay particles surface-functionalized with γ-aminopropyltriethoxysilane (γ-APTES)[33,42] were used as reactive reinforcing nanoparticles at two loading levels. The surface amine groups on the clay can participate in urea exchange reactions, increasing the density of dynamic exchange sites in the network and thereby promoting self-healing behavior.

The naming convention is as follows: PUU refers to the polyurethane–urea copolymer, while PUU-DPDS denotes PUU networks incorporating DPDS units. Samples labeled PUU-AMMT-L and PUU-DPDS-AMMT-L contain ≈3 wt% AMMT nanoclay, whereas PUU-AMMT-H and PUU-DPDS-AMMT-H contain ≈5 wt% AMMT nanoclay, based on the total sample mass.

2.3 Structural and spectroscopic characterization

The ATR-FTIR spectrum of the PUU-DPDS film is shown in Fig. S1 of the SI, which also includes the spectrum of the clay particles for comparison. The broad peak at 3344 cm^{-1} corresponds to N–H stretching, while the band at 1561 cm^{-1} is attributed to N–H bending vibrations. Peaks at 2956 cm^{-1} and 2861 cm^{-1} arise from aliphatic C–H stretching.

The band at 1714 cm^{-1} is assigned to C═O stretching of urethane groups (–NHCOO–), formed by reaction of isocyanate (–NCO) with hydroxyl (–OH) groups. The band at 1639 cm^{-1} corresponds to C═O stretching in urea groups (–NHCONH–). Importantly, no distinct peak is observed in the 2200–2300 cm^{-1} region characteristic of isocyanate groups in the cast film. This indicates that residual NCO, if present, is below the detection limit of ATR-FTIR, suggesting that unreacted isocyanate groups are present, if at all, only at low concentrations. Thus, the ATR-FTIR results are consistent with the formation of urethane and urea linkages and the absence of detectable unreacted isocyanate in the final material.

The peak at 1257 cm^{-1} is associated with both asymmetric C–O–C stretching of PEG and Si–CH_3 deformation of PDMS, confirming incorporation of both amphiphilic components. The band at 1013 cm^{-1} is assigned to Si–O–Si stretching, and the peak at 791 cm^{-1} to Si–C stretching. Contributions from C–H out-of-plane deformation of ortho-disubstituted benzene rings may also be present in this region.

X-ray diffraction provides insight into nanoparticle dispersion and structural organization within polymer matrices through changes in the interlayer spacing of clay particles. Intercalation is indicated by an increase in the basal *d*-spacing, whereas complete exfoliation leads to the disappearance of the characteristic intergallery peak. The interplanar spacing is related to the diffraction angle by Bragg's law:

$$2d\sin\theta = n\lambda \tag{5}$$

where d is the interplanar spacing, θ is the diffraction angle, n is the order of reflection, and λ is the X-ray wavelength.

Fig. 3 shows the XRD patterns of pristine PUU, PUU-DPDS, the amine-functionalized nanoclay (AMMT), and the corresponding nanocomposite samples. The AMMT clay exhibits a sharp basal reflection at $2\theta = 4.045°$, assigned to the (001) plane and corresponding to an interlayer spacing of approximately 2.18 nm, characteristic of organomodified layered silicates. Additional reflections at $2\theta \approx 19.8°$ and 21.9°, corresponding to *d*-spacings of approximately 0.448 nm and 0.405 nm, respectively, are attributed to non-basal reflections arising from in-plane crystallographic ordering within the silicate layers.

In contrast, the diffraction patterns of neat PUU and PUU-DPDS are dominated by broad diffuse halos spanning approximately 2θ = 5–25°, consistent with predominantly amorphous polymer matrices exhibiting short-range chain ordering. Within this halo, two broad features are observed near $2\theta \approx 13°$ and 21°, corresponding to *d*-spacings of approximately 0.681 nm and 0.423 nm, respectively. These features reflect short-range intermolecular correlations within the polymer matrix on the sub-nanometer scale. The higher-angle feature near 21° is associated with nearest interchain packing, potentially influenced by polar intermolecular interactions, whereas the lower-angle feature

© 2026 The Author(s). Published by the Royal Society of Chemistry

Open Access Article. Published on 27 May 2026. Downloaded on 6/18/2026 4:45:20 AM.
This article is licensed under a Creative Commons Attribution 3.0 Unported Licence.

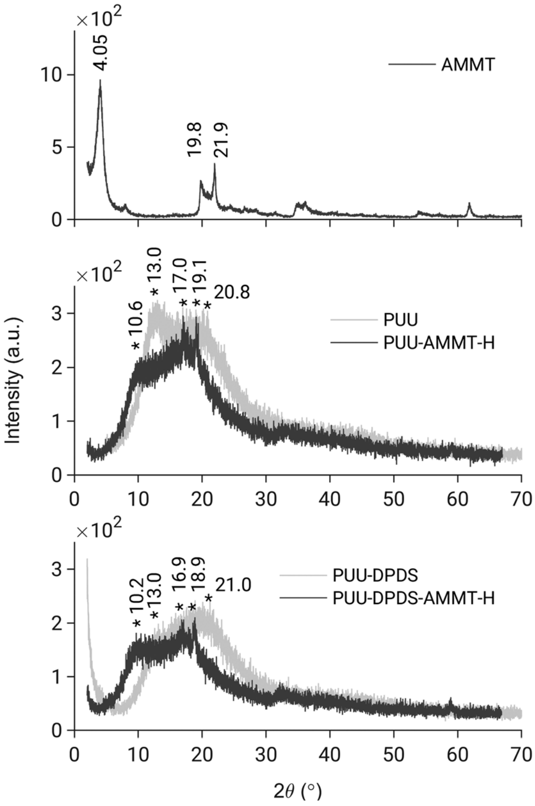

Fig. 3 X-ray diffraction patterns of pristine organoclay (AMMT), PUU, PUU-DPDS, and the corresponding nanocomposites. The pristine clay exhibits a sharp basal (001) reflection at $2\theta = 4.05°$, corresponding to an interlayer spacing of ≈2.18 nm, together with additional reflections at higher angles. In contrast, the neat PUU and PUU-DPDS matrices show broad diffuse halos, indicating predominantly amorphous structure with limited short-range order. In the nanocomposite samples, the disappearance of the clay basal reflection in the low-angle region suggests disruption of the ordered lamellar stacking of the clay layers and is consistent with extensive intercalation and/or exfoliated-disordered dispersion. Changes in the position and shape of the broad halos in the nanocomposites indicate that clay incorporation influences polymer chain packing, although the patterns remain largely amorphous.

near 13° corresponds to a larger correlation distance arising from local chain organization. Relative to PUU, PUU-DPDS shows a reduced intensity of the feature near 13° relative to that near 21°, indicating altered local packing correlations upon incorporation of aromatic disulfide units. These broad features do not provide direct information on long-range domain morphology or hard-segment spacing, which would require SAXS or related techniques.

A key feature of the nanocomposite patterns is the disappearance of the characteristic AMMT basal reflection at $2\theta \approx 4°$. In layered silicate nanocomposites, an intercalated structure typically retains a low-angle basal peak corresponding to the expanded interlayer spacing. The absence of this reflection in the present nanocomposites indicates that the regular lamellar stacking of the clay layers is largely disrupted after incorporation into the polymer matrix. The low clay content may further reduce the intensity of the basal reflection. Consequently, the disappearance of the basal reflection suggests a high degree of clay dispersion and loss of long-range interlayer registry within the polymer matrix.

The nanocomposite patterns remain dominated by broad amorphous halos, indicating that the polymer matrices retain their predominantly amorphous character after nanoclay addition. At the same time, slight changes in halo position and intensity relative to the neat polymers indicate that nanoclay incorporation influences local chain packing and short-range structural organization. Weak residual features in the $2\theta \approx 19$–$22°$ region further suggest that portions of the silicate layers retain local crystallographic order, even in the absence of long-range lamellar stacking.

2.4 Effect of disulfide linkages and nanoclay on network structure and crosslink density

Solvent swelling experiments in toluene were performed to quantify crosslinking and assess network integrity *via* measurements of gel fraction and swelling behavior.[43] Toluene was selected as the swelling solvent based on solubility-parameter considerations for the amphiphilic PEG/PDMS network. A composition-weighted Hansen solubility parameter analysis (see SI, Section S2) showed that toluene had a substantially smaller Hansen distance relative to the PEG–PDMS copolymer than more polar solvents, such as DMF and DMSO, indicating more favorable overall compatibility with both dispersive (PDMS-rich) and polar (PEG) segments. In contrast, highly polar solvents preferentially interact with polar domains and, therefore, do not uniformly probe the copolymer network, which contains a higher fraction of PDMS relative to PEG (≈0.77/0.23 by weight).

The gel fraction (w_{gel}) and swelling index (SI) were defined as:

$$w_{\text{gel}} = \frac{W_{\text{dry}}}{W_0}, \quad \text{SI} = \frac{W_{\text{swollen}}}{W_{\text{dry}}} \tag{6}$$

where W_0, W_{dry}, and W_{swollen} denote the initial, dried, and swollen masses, respectively.

Clear differences in swelling behavior were observed after 24 h. The neat PUU exhibited extensive swelling accompanied by loss of structural integrity, consistent with a high sol fraction and a loosely connected network. Incorporation of disulfide linkages improved structural coherence, although significant swelling persisted. In contrast, nanoclay-containing systems retained their macroscopic integrity, with reduced softening and minimal disintegration. The combined PUU-DPDS-AMMT system exhibited the highest stability, remaining intact with only slight deformation.

These observations were consistent with the quantitative swelling results, where the swelling index decreased and gel fraction increased with incorporation of disulfide linkages and nanoclay (Table 5), indicating a transition from a loosely connected network in PUU to a more constrained structure in the hybrid systems. Substantial swelling and nonzero sol fractions further confirmed that the materials were not fully

© 2026 The Author(s). Published by the Royal Society of Chemistry

Open Access Article. Published on 27 May 2026. Downloaded on 6/18/2026 4:45:20 AM.
This article is licensed under a Creative Commons Attribution 3.0 Unported Licence.

Table 5 Swelling and network parameters of PUU-based films in toluene after 24 h. The apparent crosslink density was estimated using the Flory–Rehner equation

Sample	Gel fraction (w_{gel})	Swelling index (SI)	ν_2	ν_e (mol cm^{-3})
PUU	0.56	5.22	0.164	6.08×10^{-5}
PUU-DPDS	0.64	3.75	0.231	1.44×10^{-4}
PUU-AMMT-H	0.79	2.96	0.296	2.83×10^{-4}
PUU-DPDS-AMMT-H	0.89	2.22	0.404	6.99×10^{-4}

crosslinked, but instead possessed finite and heterogeneous network structures. This behavior enabled solution processing while still allowing the development of significant network integrity in the final material.

The equilibrium swelling behavior was analyzed using the Flory–Rehner framework.[43] The polymer volume fraction in the swollen state (ν_2) was estimated from the measured mass uptake using polymer and solvent densities:

$$\nu_2 = \frac{W_{\text{dry}}/\rho_{\text{p}}}{\left(W_{\text{dry}}/\rho_{\text{p}}\right) + \left(W_{\text{swollen}} - W_{\text{dry}}\right)/\rho_{\text{s}}} \tag{7}$$

where $\rho_p = 1.05$ g cm^{-3} and $\rho_s = 0.867$ g cm^{-3} for toluene.

The apparent crosslink density (ν_e) was calculated as:

$$\nu_e = -\frac{\ln(1-\nu_2) + \nu_2 + \chi\nu_2^2}{V_1\left(\nu_2^{1/3} - \frac{\nu_2}{2}\right)} \tag{8}$$

where V_1 is the molar volume of toluene and $\chi = 0.45$ is an effective interaction parameter for the heterogeneous copolymer network. The ν_e values represent apparent crosslink densities and are used for comparative analysis across formulations. A monotonic increase in ν_e is observed from PUU to PUU-DPDS-AMMT (Table 5), indicating progressively increasing network constraint.

It is important to note that swelling-based estimates do not directly correspond to the true covalent crosslink density.[43] Contributions from trapped entanglements, topological constraints, and restricted chain mobility are not explicitly distinguished from covalent crosslinks within the Flory–Rehner framework, but instead may contribute collectively to the apparent network constraint inferred from swelling behavior. Accordingly, the higher ν_e observed for PUU-DPDS relative to PUU, despite a lower concentration of trifunctional crosslinker, is attributed to increased effective network constraints rather than an increase in covalent junction density. These effective constraints may arise from chain threading through network meshes and other topological restrictions, together with reduced segmental mobility and associative interactions introduced by aromatic disulfide segments, which likely persist under swelling conditions and thereby suppress solvent uptake. In addition, toluene may not fully disrupt strong polar and hydrogen-bonding interactions present in polyurethane–urea systems, further contributing to deviations from ideal Flory–Rehner behavior. The ν_e values should, therefore, be interpreted as a measure of overall network constraint under identical swelling conditions.

Swelling measurements were also conducted in water to assess network hydrophilicity. In contrast to toluene, all samples exhibited no measurable sol fraction within experimental resolution. The swelling index values were 2.59 for PUU, 1.26 for PUU-DPDS, 1.27 for PUU-AMMT-H, and 1.13 for PUU-DPDS-AMMT-H.

The reduced swelling index relative to PUU upon incorporation of DPDS and AMMT indicates decreased water uptake, consistent with increased hydrophobicity associated with the aromatic moieties of DPDS and enhanced network constraints in nanoclay-containing systems. This trend is consistent with the surface energy measurements discussed in the following section.

2.5 Surface energy determination

Surface energy components of the polymer surfaces were determined using advancing (θ_a) and receding (θ_r) contact angles of water, diiodomethane, and 1-bromonaphthalene as probe liquids, based on the Owens–Wendt–Kaelble (OWK) model (eqn (9)).

$$\frac{\gamma_{\text{L}}(1 + \cos\theta)}{2} = \sqrt{\gamma_{\text{S}}^{\text{d}}\gamma_{\text{L}}^{\text{d}}} + \sqrt{\gamma_{\text{S}}^{\text{p}}\gamma_{\text{L}}^{\text{p}}} \tag{9}$$

where γ_S^d and γ_S^p are the dispersive and polar components of the solid surface, γ_L^d and γ_L^p are those of the probe liquid, and $\gamma_L = \gamma_L^d + \gamma_L^p$. The cosine of the contact angle was obtained by averaging the advancing and receding values:[44]

$$\cos\theta = \frac{\cos\theta_{\text{a}} + \cos\theta_{\text{r}}}{2} \tag{10}$$

The surface energy components were determined by solving:

$$\mathbf{y} = \mathbf{X}\beta \tag{11}$$

where $\mathbf{y}$ is a column vector with elements $y_i = \gamma_{\text{L},i}(1 + \cos\theta_i)/2$, and $\mathbf{X}$ is an $n \times 2$ matrix (n = number of probe liquids) with elements $\sqrt{\gamma_{\text{L},i}^{\text{d}}}$ and $\sqrt{\gamma_{\text{L},i}^{\text{p}}}$ in each row. The vector β contains the unknowns $\sqrt{\gamma_S^d}$ and $\sqrt{\gamma_S^p}$ and was obtained using:

$$\beta = (\mathbf{X}^{\text{T}}\mathbf{X})^{-1}\mathbf{X}^{\text{T}}\mathbf{y} \tag{12}$$

Open Access Article. Published on 27 May 2026. Downloaded on 6/18/2026 4:45:20 AM.
This article is licensed under a Creative Commons Attribution 3.0 Unported Licence.

Table 6 Advancing, receding, and the cosine-averaged contact angles (in degrees) of probe liquids

	Water			Diiodomethane			1-Bromonaphthalene		
	θ_a	θ_r	θ	θ_a	θ_r	θ	θ_a	θ_r	θ
PUU	58	50	54	38	22	31	24	15	20
PUU-AMMT-L	81	70	75	24	14	20	13	8	11
PUU-AMMT-H	94	71	83	12	11	12	8	6	7
PUU-DPDS	71	57	64	28	17	23	20	12	17
PUU-DPDS-AMMT-L	99	64	82	16	11	14	11	7	9
PUU-DPDS-AMMT-H	102	91	96	12	3	9	6	5	6

The surface energy components γ_S^d and γ_S^p were obtained by squaring the corresponding elements of β, and the total surface energy was calculated as $\gamma_S = \gamma_S^d + \gamma_S^p$.

Experimental contact angle values and probe liquid parameters are listed in Table 6, and the resulting surface energy components are summarized in Table 7. Fig. 4 presents a parity plot comparing experimental and model values of **y**, showing good agreement.

It is seen from the values in Table 7 that the polar component of the surface energies of the PUU surfaces decreased with an increase in the concentration of the surface-functionalized nanoclay in the composites, attributed to the surface functionalization of the clay particles with the relatively nonpolar alkyl groups. The dispersion components showed a corresponding increase. The PUU-DPDS surfaces had a significantly lower polar component of surface energy. Evidently, the nonpolar PDMS segments of the polymers dominate the surface energy of these materials. Consequently, the polar contribution to the surface energy was low, and the total surface energy was lower for PUU-DPDS than for PUU.

2.6 Thermophysical characterization

DSC glass transition behavior. The glass transition temperature of the elastomers, determined by DSC, appeared as a step change in heat flow. To accurately identify the transition, a derivative plot of heat flow *versus* temperature was used, where T_g corresponds to the peak of the inflection point (Fig. 5). The observed T_g values were within the range

Table 7 Dispersion and polar components, and total surface energy, in mJ m^{-2}, of probe liquids and polymer surfaces

Liquid	γ_d	γ_p	γ
Water	21.8	51.0	72.8
Diiodomethane	49.5	1.3	50.8
1-Bromonaphthalene	44.4	0	44.4
PUU	39.2	15.7	54.9
PUU-AMMT-L	42.0	9.5	51.5
PUU-AMMT-H	44.1	4.2	48.3
PUU-DPDS	46.0	1.8	47.8
PUU-DPDS-AMMT-L	45.6	2.0	47.6
PUU-DPDS-AMMT-H	47.7	0.0	47.7

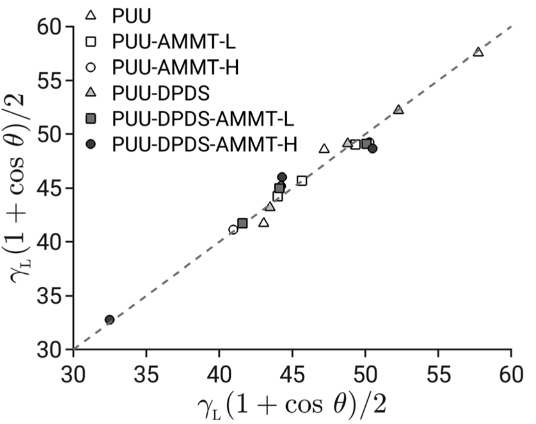

Fig. 4 Parity plot for surface energy determination using θ, the experimental contact angles. $\hat{\theta}$ is the contact angle predicted by the OWK model.

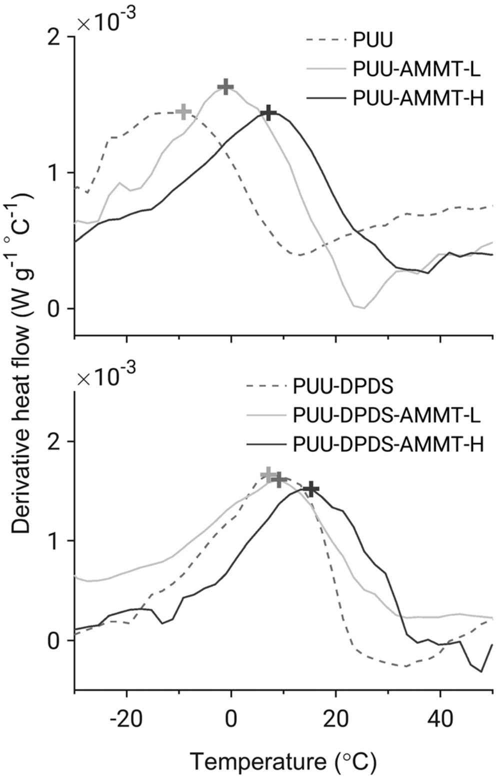

Fig. 5 Derivative of heat flow *versus* temperature for PUU and PUU-based nanocomposites, showing inflection points corresponding to the glass transition.

© 2026 The Author(s). Published by the Royal Society of Chemistry

Open Access Article. Published on 27 May 2026. Downloaded on 6/18/2026 4:45:20 AM.
This article is licensed under a Creative Commons Attribution 3.0 Unported Licence.

of −30 to 30 °C. PUU-DPDS exhibited a markedly higher T_g (8.4 °C) than PUU (−9.9 °C), indicating increased rigidity arising from the incorporation of diphenyl disulfide groups. Incorporation of nanoclay (AMMT) further elevated T_g by restricting segmental mobility through polymer–clay interactions. A consistent increase was observed with higher clay content: from −9.9 °C (PUU) to −0.76 °C (PUU-AMMT-L) and 6.8 °C (PUU-AMMT-H); and from 8.4 °C (PUU-DPDS) to 14.4 °C (PUU-DPDS-AMMT-H).

DMA temperature sweep. DMA temperature-sweep measurements were performed to probe the temperature-dependent viscoelastic response of representative films. The corresponding storage modulus (E') and loss modulus (E'') profiles are provided in SI (Fig. S2). The glass transition temperatures, estimated from the onset of the decrease in E', were −24.8 °C for PUU, −10.2 °C for PUU-DPDS, and 31.6 °C for PUU-DPDS-AMMT-H. These results show the same qualitative trend as DSC, with an increase in T_g upon incorporation of aromatic disulfide linkages and nanoclay, consistent with increased network constraints and reduced chain mobility. However, the T_g values obtained from DMA and DSC differ for a given sample, as the techniques probe distinct manifestations of the glass transition—mechanical relaxation in DMA, and heat capacity in DSC—and are, therefore, not directly comparable.[45]

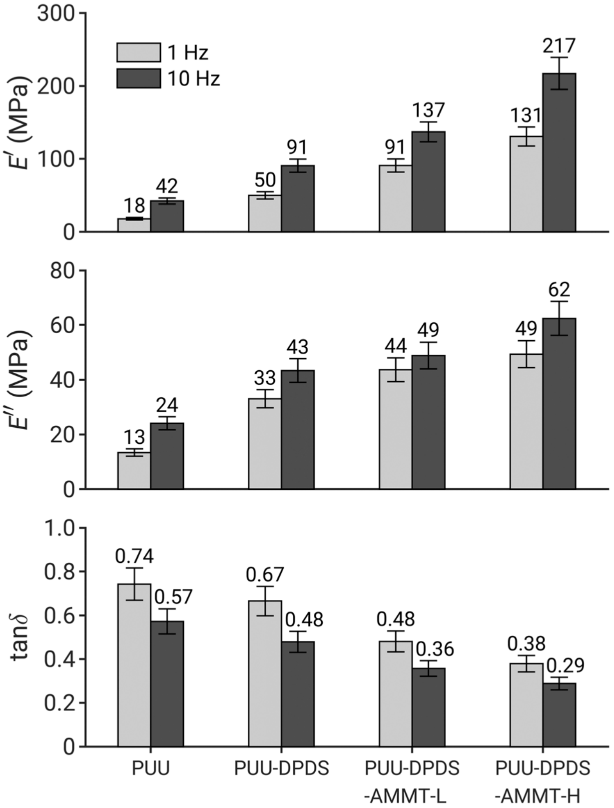

Fig. 6 Frequency sweep DMA results at 26 °C showing storage modulus (E'), loss modulus (E''), and loss tangent (tan δ) for the PUU-DPDS systems. Data are compared at 1 and 10 Hz.

DMA frequency sweep. Fig. 6 shows the storage modulus (E'), loss modulus (E''), and loss tangent (tan $\delta = E''/E'$) from frequency sweep DMA conducted at ≈25 °C. The figure compares these parameters for the three PUU-DPDS films at 1 and 10 Hz, where low- and high-frequency values represent responses to slow and rapid strain variations, respectively. A corresponding chart for PUU is provided in the SI (Fig. S3), and the full frequency-dependent curves (0.1–100 Hz) for both PUU and PUU-DPDS systems are included in the SI (Fig. S4 and S5).

Both PUU and PUU-DPDS exhibited an increase in E' with frequency. PUU-DPDS demonstrated more than a twofold higher E' than PUU (50 MPa *vs.* 18 MPa at 1 Hz and 91 MPa *vs.* 42 MPa at 10 Hz), indicating enhanced rigidity imparted by aromatic disulfide linkages. Incorporation of nanoclay further improved stiffness and elasticity. A pronounced decrease in tan δ with increasing clay concentration, particularly in PUU-DPDS-AMMT-H, reflected reduced energy dissipation and enhanced load-bearing capacity.

Structure–property relationships and mechanical implications. The combined incorporation of disulfide linkages and organoclay leads to a marked increase in storage modulus accompanied by a reduction in damping (tan δ), indicating restricted segmental mobility. Consequently, the elastomer network exhibits enhanced elastic energy storage with reduced dissipative losses. In conventional self-healing polymers, increased T_g and reduced tan δ are typically associated with slower healing due to limited chain mobility at damaged interfaces. In contrast, nanoclay incorporation significantly accelerates healing kinetics.

Despite the increase in modulus and T_g, incorporation of nanoclay enhanced healing performance (*vide infra*), indicating that healing in the present system is not governed by segmental mobility alone. The concurrent increases in T_g, storage modulus, and gel fraction upon nanoclay incorporation indicate enhanced network connectivity together with more restricted chain mobility. Swelling measurements (Table 5) show a systematic increase in gel fraction with nanoclay addition, consistent with polymer–filler interactions contributing to network structure rather than inert filler behavior.

Importantly, the increase in gel fraction (for example, from 0.64 to 0.89 for PUU-DPDS) substantially exceeds the maximum clay mass fraction in the composite (≈0.05), indicating that the effect cannot be attributed solely to the physical presence of clay particles. Rather, nanoclay appears to promote additional network formation and an increase in effective crosslink density, as also reflected in Table 5. In this sense, the clay functions as a reactive crosslinking site within the polymer network. This behavior is consistent with interactions between amine-functionalized clay surfaces and isocyanate groups, together with possible participation in dynamic urea exchange processes.

These observations indicate that nanoclay influences network dynamics beyond purely mechanical reinforcement.

© 2026 The Author(s). Published by the Royal Society of Chemistry

Open Access Article. Published on 27 May 2026. Downloaded on 6/18/2026 4:45:20 AM.
This article is licensed under a Creative Commons Attribution 3.0 Unported Licence.

The improved healing performance despite reduced mobility is therefore consistent with an increased availability or effectiveness of dynamic bond-exchange pathways.

This behavior may also be understood in the context of the microphase organization characteristic of segmented polyurethane–urea systems.[46] Differences in polarity and hydrogen-bonding interactions between PEG/PDMS-rich soft segments and urethane/urea/aromatic disulfide-rich hard regions promote phase-separated morphologies that govern segmental mobility and mechanical response. Within this framework, nanoclay may preferentially associate with the more polar hard domains, reinforcing these regions while preserving sufficient mobility within the soft phase for healing. Such selective reinforcement could help reconcile increased stiffness with efficient self-healing.

The tensile properties of unfilled PUU and PUU-DPDS are presented in Fig. S6 of the SI. Although PUU-DPDS exhibits a higher storage modulus than PUU in DMA measurements, its yield strength under uniaxial tension is lower. This reflects the distinct roles of covalent crosslinking and segmental rigidity. The PUU formulation contains approximately twice the amount of trifunctional crosslinker relative to PUU-DPDS to ensure adequate film stiffness, contributing to its higher yield strength. In contrast, the storage modulus is influenced more strongly by segmental stiffness. The aromatic disulfide units in PUU-DPDS increase segmental rigidity, resulting in a higher storage modulus despite the lower crosslinker content.

2.7 Recovery *via* reversible bond dynamics

Li *et al.*[31] quantified underwater healing kinetics using a notch-recovery experiment in which a defined scratch was introduced into the film and monitored under immersion by optical and confocal microscopy. The healing speed was calculated as the ratio of the initial notch depth (0.4 mm) to the time required for complete visual disappearance of the scratch, yielding an average geometric recovery rate of 33 μm h^{-1}.

In the present study, optical microscopy was similarly used to monitor the closure of cuts in the films under immersion. However, we found that visual disappearance of the notch did not directly correspond to recovery of mechanical strength. In several instances, the damaged region appeared optically healed while tensile properties remained only partially restored. This observation indicates that surface-level gap closure can precede full reconstruction of load-bearing network connectivity through reversible bond exchange. Consequently, mechanical testing was necessary to assess true structural recovery beyond geometric crack sealing.

Healing at the crack interface was quantified using tensile testing. Intact and cut-rejoined specimens were compared across different film compositions, temperatures, and healing environments (air or water). After cutting, the samples were carefully rejoined without external pressure and allowed to heal for up to 24 h. The self-healing process of the PUU and PUU-DPDS elastomers after cutting is shown in Video S1 (SI). Healing efficiency was determined by comparing the stress–strain response of healed specimens with that of the original intact samples, enabling the influence of molecular design, temperature, and medium on mechanical strength recovery to be assessed. Representative stress–strain curves for PUU-DPDS films healed underwater at 30 °C for 24 h are shown in Fig. 7.

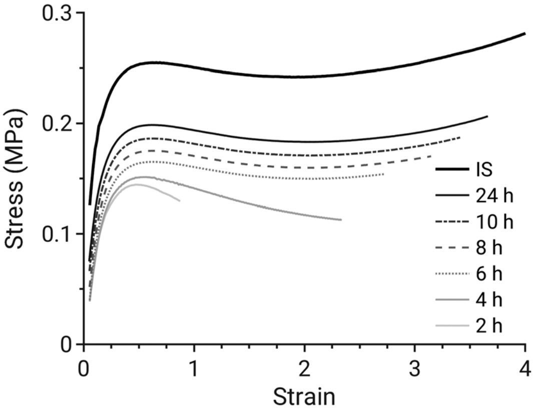

Fig. 7 Evolution of stress–strain plots during healing of cut PUU-DPDS underwater at 30 °C, and comparison with an intact sample (IS). Stress values at 0.5 strain, indicated by dotted vertical line, were analyzed.

Healing metrics. To quantify healing, two metrics were extracted from the stress–strain curves: (1) toughness, defined as the area under the stress–strain curve up to fracture or, if the specimen did not fracture, up to the maximum applied strain (≈4); and (2) the stress at a strain of 0.5, representing interfacial strength under load. These parameters were measured every 2 h during the first 10 h of healing and again after 24 h.

For normalization, reference values were obtained from uncut samples, defined as the toughness at a strain of 4 and the stress at a strain of 0.5. Healing performance was expressed as the percent recovery relative to these reference values. Reported values represent averages from at least two independent measurements performed using separate batches of each formulation.

Fig. 8 presents the final recovery of toughness and strength in PUU and PUU-AMMT-H films after 24 hours of healing at two temperatures, 30 and 60 °C, under both air and water environments. Several key trends are immediately apparent and consistent for both toughness and strength recovery: (1) healing in water results in significantly lower recovery than in air; (2) higher temperatures (60 °C) promote greater recovery than lower temperatures (30 °C). (3) Strength recovery consistently exceeds toughness recovery.

Most notably, the incorporation of AMMT nanoclay particles substantially enhanced healing performance. This is particularly striking given that PUU-AMMT-H exhibited a much higher storage modulus, ≈104 MPa at 1 Hz (*cf.* Fig. S3, SI), more than five times greater than unfilled PUU (≈18 MPa). The fact that healing was accelerated

© 2026 The Author(s). Published by the Royal Society of Chemistry

Open Access Article. Published on 27 May 2026. Downloaded on 6/18/2026 4:45:20 AM.
This article is licensed under a Creative Commons Attribution 3.0 Unported Licence.

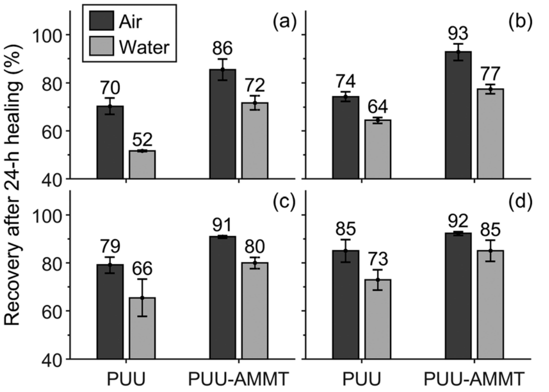

Fig. 8 Recovery of toughness (a and c) and strength (b and d) for PUU and PUU-AMMT-H films after 24-hour healing at 30 °C (a and b) and 60 °C (c and d), in air and underwater environments.

despite this considerable increase in stiffness is both unexpected and remarkable, suggesting a synergistic role of the nanoclay in facilitating interfacial mobility or network reformation during healing.

Similar trends were observed for the PUU-DPDS-based films. Fig. 9 shows the time evolution of toughness and strength recovery during healing at 30 °C in both air and water. Bar charts compare the percent recovery at 8 and 24 hours for the neat copolymer and for composites incorporating low (≈3 wt%) and high (≈5 wt%) loadings of AMMT clay nanoparticles. The corresponding results for healing at 60 °C are presented in Fig. S7.

As in the case of PUU, strength recovery consistently exceeds toughness recovery, healing is more effective in air than in water, and recovery improves with increasing clay content. Notably, this enhancement occurs despite a substantial increase in film stiffness with higher AMMT loading (*cf.* Fig. 6), highlighting the unusual yet beneficial role of nanoclay in promoting self-healing.

These findings are noteworthy in the broader context of urea-based polymer networks. Conventional urea linkages have been regarded as highly stable because of strong resonance stabilization of the amide bond, which generally suppresses reversible dissociation under typical conditions. Wang *et al.*[13] reported that Lewis-acid catalysts such as Zn^{2+} at elevated temperatures are required to activate urea bonds formed from primary amines to undergo reversible dissociation and exchange. In their study, simple dialkyl urea model compounds (*e.g.*, *N*,*N*′-diethylurea) were examined. Coordination of Zn^{2+} to the urea carbonyl lowers the barrier for dissociation into isocyanate and amine intermediates,

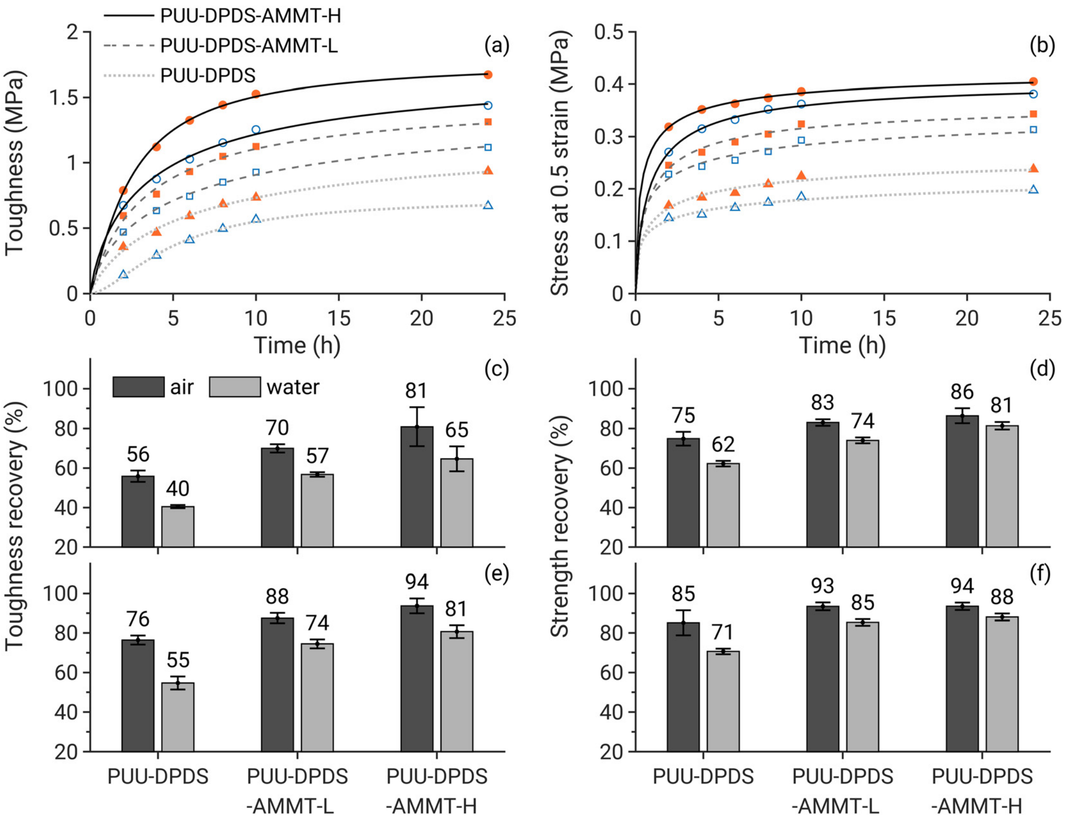

Fig. 9 Toughness and strength recovery of PUU-based films during healing at 30 °C in air and underwater environments. ○ = PUU-DPDS-AMMT-H, □ = PUU-DPDS-AMMT-L, △ = PUU-DPDS. Panels (a and b) show the time evolution of toughness and stress at a strain of 0.5 (taken as a measure of strength), respectively; blue unfilled symbols represent underwater healing, whereas orange filled symbols correspond to healing in air. Panels (c and d) show toughness and strength recovery after 8 hours, and panels (e and f) show recovery after 24 hours. Recovery in panels (c–f) is expressed as a percentage relative to the intact (uncut) specimen.

Open Access Article. Published on 27 May 2026. Downloaded on 6/18/2026 4:45:20 AM.
This article is licensed under a Creative Commons Attribution 3.0 Unported Licence.

enabling thermally activated bond exchange and self-healing in polyurea networks at ≈90 °C on timescales of tens of minutes to hours.

However, the importance of steric modification of the urea linkage in enabling dynamic urea exchange, such as the phenyl substituents present in our PUU-DPDS copolymers, is evident from the work of Ying *et al.*[12] Bulky substituents on the urea nitrogen reduce the resonance stabilization of the C–N bond, thereby facilitating reversible dissociation into isocyanate and amine intermediates without the need for added catalysts. Polyurethane–urea networks incorporating such sterically hindered urea motifs exhibit autonomous self-healing near ambient temperature while retaining the mechanical integrity of the crosslinked network.

Neither study examined healing in aqueous or underwater environments. In contrast, the significant healing observed in the present PUU-based materials occurs without the addition of catalytic species and remains measurable under underwater conditions (see Fig. 8). These observations are consistent with our DFT calculations, which show that the activation barrier for urea exchange is substantially lower than that for urethane exchange in both vacuum and aqueous environments (see Table 1), supporting the ability of urea linkages to participate in bond rearrangement under the conditions studied.

Origin of discrepancy between stress and toughness recovery. The consistently lower recovery in toughness relative to stress at 0.5 strain reflects the distinct structural requirements associated with these metrics. Recovery of stress at 0.5 strain primarily depends on restoration of load-bearing continuity across the healed interface, which can be achieved through relatively localized processes such as dynamic covalent exchange (for example, disulfide metathesis or urea exchange) and short-range interfacial reconnection. As observed in Fig. 9, this recovery is particularly effective in the clay-containing samples, resulting in high stress recovery at relatively short healing times.

By contrast, toughness is an energy-based measure that depends on the full deformation process, including large-strain extensibility, strain hardening, and resistance to crack initiation and propagation. Its recovery, therefore, requires more extensive structural reconstruction, including chain interpenetration across the healed interface, restoration of network continuity, and reduction of residual defects and weakly connected regions at the healed interface. These processes are slower and more sensitive to the degree of interfacial healing.

This interpretation is consistent with the classical framework of polymer interface mechanics. Brown[47] showed that interfacial fracture toughness (G_c) increases with the density of load-bearing chain segments spanning the interface and remains limited when interfacial molecular connectivity is underdeveloped. In this regime, reduced interfacial connectivity restricts stress transfer and energy dissipation during crack propagation, even when some interfacial bonding is present.

Therefore, in the present system, while dynamic bond exchange enables relatively rapid recovery of stress at 0.5 strain through local interfacial reconnection, the slower development of broader interfacial connectivity and network reorganization limits the recovery of toughness. This is consistent with the lower toughness recovery observed in Fig. 9c relative to the stress recovery shown in Fig. 9d.

Kinetic analysis. To quantify healing kinetics, the recovery *vs.* time data acquired during the initial stages of healing (up to 8 hours) were fitted to the expression:

$$R = 0.5\left(\frac{t}{\tau_{1/2}}\right)^{\alpha} \qquad (13)$$

where $\tau_{1/2}$ is the time required to reach 50% recovery, and α is a kinetic exponent. Fig. 10 shows the fits to the toughness recovery data, which exhibit good agreement with the model. The corresponding values of the fit parameters are presented in Fig. 11.

The results clearly show that $\tau_{1/2}$ decreases significantly with increasing clay content. For instance, at 30 °C in air, the time to 50% recovery of toughness decreased from approximately 4.5 h for the neat PUU-DPDS film to just 0.7 h for the composite containing 5 wt% AMMT. The exponent α remained relatively constant for the PUU-DPDS-AMMT composites, ranging from approximately 0.22 to 0.29, but was notably higher for the neat copolymer, indicating a faster early-stage recovery behavior.

Fig. S8 in the SI presents the kinetic analysis of toughness recovery at 60 °C, while Fig. S9–S11 show strength recovery at 30 and 60 °C, in air and water, for the PUU-DPDS systems.

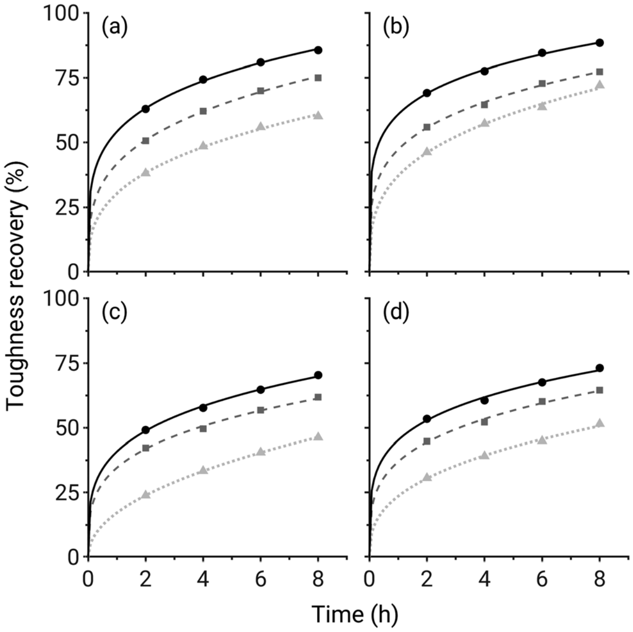

Fig. 10 Toughness recovery of cut samples healed at: (a) 30 °C in air, (b) 60 °C in air, (c) 30 °C in water, and (d) 60 °C in water. 100% corresponds to the toughness of the original intact specimen. ○ = PUU-DPDS-AMMT-H, □ = PUU-DPDS-AMMT-L, △ = PUU-DPDS.

© 2026 The Author(s). Published by the Royal Society of Chemistry

Open Access Article. Published on 27 May 2026. Downloaded on 6/18/2026 4:45:20 AM.
This article is licensed under a Creative Commons Attribution 3.0 Unported Licence.

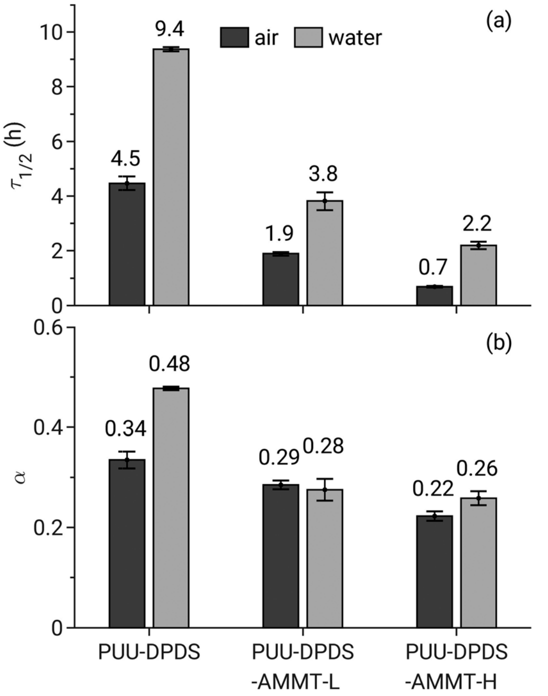

Fig. 11 Fitted parameters (a) $\tau_{1/2}$ and (b) α from the power-law model describing toughness recovery over time for neat PUU-DPDS and its AMMT composites during healing in air and under water at 30 °C

Fig. S12 and S13 present the corresponding toughness and strength recovery kinetic parameters for the PUU systems.

Role of disulfide bonds. PUU-DPDS, containing dynamic disulfide bonds, exhibited faster and more complete healing than PUU. It recovered over 76% of its original toughness within 24 h (Fig. 9e), whereas PUU showed lower recovery (70%; see Fig. 8a). More significantly, the half-healing time ($\tau_{1/2}$) for PUU-DPDS was 4.5 h in air at 30 °C, compared to 7.4 h for PUU (Fig. S12, SI), underscoring the role of reversible disulfide exchange in facilitating faster healing at room temperature. These trends were consistent in both air and water, though healing was generally slower and less complete under water.

PUU-DPDS exhibits superior healing due to reversible disulfide metathesis, which reconnects polymer chains across the fracture interface. These dynamic covalent bonds are thermally activated at ambient temperature, enabling efficient healing through new covalent bond formation at the crack site. In contrast, PUU lacks disulfide-based dynamic covalent chemistry and relies solely on reversible urea interactions, which provide limited mechanical recovery.

Effect of water on healing kinetics. All data presented thus far indicate that recovery driven by dynamic covalent exchange is slower in water than in air. As shown in Fig. 8a, PUU achieved 70% toughness recovery after 24 hours of healing in air at 30 °C, but only 52% in water. As previously discussed, incorporation of DPDS enhanced recovery (Fig. 9e) in both environments. Recovery further improved with the addition of clay particles to the films. Specifically, Fig. 9e shows that the PUU-DPDS-AMMT-H film achieved 94% recovery in air and 81% in water.

This behavior suggests that while urea and aromatic disulfide-based dynamic covalent exchanges remain active in aqueous environments, their reaction rates are reduced at a given temperature. Although water-induced plasticization of the polymer network may enhance chain mobility and facilitate healing, the inhibitory effect of water on dynamic covalent bond exchange appears to dominate over the benefits of increased molecular diffusion. This is reflected in the relatively low toughness recovery observed under water (52% for PUU and 55% for PUU-DPDS). These results indicate that water alone cannot promote healing in the absence of dynamic covalent interactions.

Enhancement of self-healing by organoclay. Fig. 11 demonstrates that amine-functionalized MMT clay nanoparticles significantly accelerate toughness recovery in both air and underwater environments. This enhancement can be attributed to several factors: (1) reactive amine groups on the clay surface engage in dynamic covalent exchange with urea bonds, facilitating network reformation; (2) increased hydrophobicity from clay incorporation (see water contact angles in Table 6) reduces water diffusion into the films, thereby promoting urea exchange reactions despite a concomitant reduction in water-induced plasticization; and (3) the high interfacial area provided by the two-dimensional clay filler enables effective dissipation of fracture energy, inhibiting crack propagation. Remarkably, although the clay particles increase film stiffness, they simultaneously accelerate healing rates in both air and aqueous conditions, highlighting their promising role in enhancing self-healing performance.

3 Conclusions

Achieving autonomous self-healing in polyurethane coatings under aqueous conditions remains challenging, as water interferes with chain diffusion and dynamic bond exchange, while reinforcing fillers typically suppress healing by restricting polymer mobility. In this work, amphiphilic polyurethane–urea networks incorporating PEG and PDMS segments were designed to enable autonomous self-healing in both air and underwater environments. The base PUU system exhibited substantial toughness recovery, reaching approximately 70% in air and 52% underwater after 24 h at 30 °C, enabled by dynamic urea exchange. Incorporation of ≈3.3 wt% 4,4′-diaminodiphenyl disulfide, close to the upper limit for maintaining elastomeric behavior, further improved recovery to approximately 76% in air and 55% underwater, reflecting the additional contribution of disulfide exchange.

A more pronounced enhancement in both the rate and extent of healing was achieved through incorporation of amine-functionalized montmorillonite nanoclay. Despite a substantial increase in network modulus, the nanoclay accelerated healing kinetics, mitigating the conventional trade-off between stiffness and self-healing. The best-performing nanocomposite exhibited near-complete mechanical recovery, with toughness reaching approximately 94% in air and 81% underwater after 24 h at 30 °C.

Open Access Article. Published on 27 May 2026. Downloaded on 6/18/2026 4:45:20 AM.
This article is licensed under a Creative Commons Attribution 3.0 Unported Licence.

Density functional theory calculations provided a molecular-level framework by establishing the energetic hierarchy of dynamic bond exchange reactions. Urea and disulfide exchange were kinetically accessible under moderate conditions, whereas urethane exchange exhibited significantly higher activation barriers. These findings were consistent with the experimental observation that urea and disulfide linkages enabled effective network rearrangement, even in aqueous environments.

Incorporation of reactive nanoclay nanoparticles enabled simultaneous reinforcement of polyurethane–urea networks and facilitated dynamic bond exchange at damaged interfaces, providing a design strategy for developing mechanically robust, self-healing coatings capable of sustained performance in aqueous and submerged environments.

Future work should directly probe healing at polymer–nanoclay interfaces using spectroscopic methods and localized mechanical measurements, such as nanoindentation, to clarify how surface functionalities influence dynamic bond exchange and interfacial recovery. Stress-relaxation analysis, widely used to characterize reversible polymer networks,[5,23] would further quantify relaxation times and activation energies associated with network rearrangement. These complementary approaches would provide a more rigorous link between molecular-scale exchange dynamics and macroscopic self-healing behavior, as demonstrated in dynamic covalent and vitrimer networks.[8]

4 Materials and methods

4.1 DFT analysis of dynamic covalent bond activation energies in gas-phase and aqueous environments

DFT calculations were performed using Gaussian 16 to elucidate reaction pathways and activation free energies associated with dynamic covalent bond-exchange processes in gas-phase and aqueous environments. All stationary points were initially optimized at the B3LYP/6-31+G(d,p) level of theory, which provides a balance between computational efficiency and thermochemical reliability for organic systems.[48] To validate the robustness of the calculated energetics, key stationary points and activation barriers were re-evaluated using the range-separated, dispersion-corrected hybrid functional ωB97X-D with the def2-TZVP basis set.[49] Both functionals yielded consistent mechanistic trends and comparable activation energies, indicating that the conclusions are not sensitive to the choice of functional.

Solvent effects were modeled using the SMD continuum solvation model, and all structures were optimized in both gas-phase and aqueous environments. Harmonic vibrational frequency analyses were performed to characterize stationary points. True minima (reactants, intermediates, and products) were confirmed by the absence of imaginary frequencies, while transition states were identified by a single imaginary frequency corresponding to motion along the reaction coordinate.

Intrinsic reaction coordinate (IRC) calculations were performed for each transition state to confirm connectivity between adjacent minima and to distinguish between concerted and stepwise pathways.

Thermodynamic and kinetic parameters, including activation free energies ($\Delta G^{\ddagger}$), reaction enthalpies (ΔH), and overall Gibbs free energy changes (ΔG), were obtained from frequency calculations at 298.15 K and 1 atm under the ideal-gas, rigid-rotor, and harmonic-oscillator approximations. Gibbs free energy was computed as

$$G = E_{\text{elec}} + E_{\text{ZPE}} + \Delta E_{\text{thermal}} - TS \tag{14}$$

where E_{elec} is the electronic energy, E_{ZPE} is the zero-point energy, $\Delta E_{\text{thermal}}$ represents thermal corrections to enthalpy, and S is the entropy. Solution-phase free energies were corrected from the gas-phase standard state (1 atm) to a solution standard state of 1 M. All reported energies correspond to stationary points verified by vibrational analysis and IRC connectivity.

4.2 Materials

α,ω-Dihydroxy-telechelic poly(ethylene glycol) (PEG, CAS No. 25322-68-3, $M_n \approx 400$ g mol^{-1}, Beantown Chemicals), isophorone diisocyanate (IPDI, CAS No. 4098-71-9, 222.28 g mol^{-1}, Acros Organics, 98%), di-*n*-butyltin dilaurate (DBTDL, CAS No. 77-58-7, 631.56 g mol^{-1}, Alfa Aesar, 95%), bis(3-aminopropyl)-terminated polydimethylsiloxane (PDMS, CAS No. 106214-84-0, $M_n \approx 875$ g mol^{-1}, Gelest), trimethylolpropane tris[α-hydroxy-ω-amino-poly(propylene glycol)] ether (CAS No. 39423-51-3, $M_n \approx 440$ g mol^{-1}, Sigma-Aldrich), 4,4′-diaminodiphenyl disulfide (APDS, CAS No. 722-27-0, 248.36 g mol^{-1}, TCI America, >98.0%), and tetrahydrofuran (THF, 99.9%, extra dry, Acros Organics) were used as received. Amine-functionalized montmorillonite (AMMT, Nanomer I.31PS) was obtained from Nanocor, Inc. (Hoffman Estates, IL). 1-Bromonaphthalene (CAS No. 90-11-9, Alfa Aesar, 97%) and diiodomethane (CAS No. 75-11-6, Alfa Aesar, >99%) were used for contact angle measurements.

4.3 Polymer synthesis and film preparation

PUU and PUU-DPDS copolymers were synthesized *via* a two-step solution polymerization in anhydrous THF under nitrogen. Reactions were conducted in a three-neck round-bottom flask equipped with a reflux condenser and magnetic stirring. The system was maintained under a continuous nitrogen atmosphere and remained closed throughout. All reagents were introduced *via* syringe through septa.

In a typical procedure, IPDI and α,ω-dihydroxy PEG ($M_n \approx 400$ g mol^{-1}) were dissolved separately in anhydrous THF to form 20 wt% solutions. The PEG solution contained DBTDL catalyst (≈0.2 wt% relative to the combined mass of IPDI and PEG). The solutions were combined under nitrogen and heated at 75 °C for 3 h to form an isocyanate-terminated

© 2026 The Author(s). Published by the Royal Society of Chemistry

Open Access Article. Published on 27 May 2026. Downloaded on 6/18/2026 4:45:20 AM. This article is licensed under a Creative Commons Attribution 3.0 Unported Licence.

prepolymer. Solvent loss during reflux was monitored and minimized by controlled nitrogen flow, and THF was replenished as needed *via* syringe.

The reaction mixture was cooled to ∼30–35 °C over 45–60 min while maintaining the nitrogen atmosphere. A THF solution (20 wt%) of diamino-terminated PDMS ($M_n \approx 875$ g mol^{-1}), with or without bis(4-aminophenyl) disulfide (APDS), was added dropwise under stirring. After 15–20 min, a THF solution of the trifunctional amine crosslinker (trimethylolpropane tris[α-hydroxy-ω-amino-poly(propylene glycol)] ether) was added dropwise, and the reaction was continued for an additional 1 h.

The resulting viscous solution was cast into PTFE molds using a pipette, with care taken to minimize bubble formation and ensure uniform films. The cast solutions were placed under a gentle vacuum for 15 min to remove trapped air bubbles. Samples were dried at room temperature for ≈24 h, followed by further drying at 60 °C for 3 h to remove residual solvent, yielding elastomeric films. The material remained processable in THF prior to film formation, enabling homogeneous mixing.

The molar compositions of the formulations are provided in Table 4. PUU-DPDS samples contained APDS, whereas PUU samples did not. The total amine functionality from APDS and the trifunctional crosslinker, together with the hydroxyl functionality of PEG, was designed to match the isocyanate functionality of IPDI, ensuring near-stoichiometric equivalence.

Preparation of polymer–clay composite films. For nanocomposite samples, γ-APTES-functionalized montmorillonite (MMT, Nanomer I.31PS) was dried under vacuum at 60 °C for 24 h. The nanoclay was dispersed in THF (10 wt%) by ultrasonication (55% amplitude, 3 s pulse, 1 s pause, 5 min) to obtain a homogeneous suspension. This dispersion was combined with the polymer solution to achieve clay loadings of 3 or 5 wt%, followed by stirring at room temperature for 1 h. The mixtures were cast into PTFE molds and dried at room temperature for 24 h, followed by vacuum drying at 60 °C for 5 h.

4.4 Materials characterization

FTIR-ATR. Spectra were collected using a Thermo Fisher Nicolet iS10 with an ATR accessory at room temperature, averaging 32 scans at 4 cm^{-1} resolution over 4000–400 cm^{-1}.

X-ray diffraction. A Malvern Panalytical X'PERT PRO MRD diffractometer equipped with a Cu Kα source (1.8 kW Cu anode), Bragg–Brentano θ–2θ geometry, and a PIXcel3D detector was used to obtain diffraction patterns of PUU, PUU-DPDS, and PUU-DPDS-AMMT films, and of AMMT clay by powder diffraction. Bulk samples (1–2 mm thick discs) were used for the films. Measurements were conducted at room temperature at 45 kV and 40 mA using Cu Kα radiation (λ = 0.154 nm). Data were collected over a 2θ range of 2° to 70° with a step size of 0.01°.

Solvent swelling measurements. Polymer samples were dried to constant weight at 40 °C and weighed to obtain the initial mass (W_0), then immersed in toluene for 24 h at room temperature. After swelling, samples were removed (PUU by filtration; others using tweezers), blotted, and weighed to obtain the swollen mass (W_{swollen}), then dried at 40 °C overnight and reweighed to obtain the final dry mass (W_{dry}). Gel fraction and swelling index were calculated from these measurements. Experiments were repeated in water. Measurements were conducted in triplicate. The relative standard deviation was below 5% for swelling index and gel fraction. Variability primarily arises from estimation of W_{swollen} due to solvent loss during handling and blotting.

Differential scanning calorimetry. Thermal transitions and curing behavior of the polymer films were analyzed by DSC (DSC 3+, Mettler-Toledo) under nitrogen. Samples (5–15 mg) were sealed in aluminum pans, with an empty sealed pan as reference. Two heating–cooling cycles were performed from −80 to 80 °C at 10 °C min^{-1}, and heat flow was recorded as a function of temperature.

Dynamic mechanical analysis. DMA was performed using a TA Instruments Q850 in tension mode. Rectangular specimens were cut from the films. Frequency sweeps were conducted at a strain amplitude of 0.1% over 0.1–100 Hz at ≈25 °C. Temperature sweeps were performed at 1 Hz and ≈0.1% strain (within the linear viscoelastic regime) from −80 to 40 °C at 3 °C min^{-1}, with storage and loss moduli recorded as functions of temperature.

Contact angle measurements. Contact angles were measured by the sessile drop method using a Model 100-00 Rame-hart goniometer (Rame-hart Instrument Co., Netcong, NJ) with a 22-gauge stainless steel needle (0.7 mm o.d., 0.4 mm i.d.). Advancing and receding angles were determined under ambient conditions by controlled addition and withdrawal of the probe liquid.

Tensile testing and healing protocol. Stress–strain measurements were performed using a Q850 DMA with a tension clamp at ≈25 °C and a crosshead speed of 50 mm min^{-1}. Rectangular specimens (nominally 2 mm wide and 1 mm thick) were cut from the films, and mechanical properties were measured for both intact and healed specimens. Healed samples were prepared by cutting specimens at the midpoint with a razor blade and bringing the cut surfaces into contact without external pressure (see Video S1, SI). Healing was conducted in air and water at 30 °C and 60 °C for 2–24 h. For underwater healing, films were immersed in deionized water at the specified temperature; at each time point, specimens were removed, gently dried, and immediately tested. Healing efficiency was quantified from the stress at 50% strain and toughness relative to uncut controls. DMA force and displacement limits (18 N and ∼25 mm) were considered in selecting specimen dimensions and test conditions.

Author contributions

R. A.: methodology, investigation, writing – original draft. M. B.: methodology, validation, investigation, data curation, writing – original draft. S. K.: conceptualization, methodology, formal

Open Access Article. Published on 27 May 2026. Downloaded on 6/18/2026 4:45:20 AM.
This article is licensed under a Creative Commons Attribution 3.0 Unported Licence.

analysis, visualization, supervision, writing – review and editing, funding acquisition.

Conflicts of interest

There are no conflicts to declare.

Data availability

Data supporting this study are available within the article or from the corresponding author upon request.

Supplementary information (SI): Flory–Stockmayer gelation analysis; ATR-FTIR characterization; dynamic mechanical analysis (temperature sweeps and frequency-dependent viscoelastic response); representative stress–strain curves; additional self-healing data in air and underwater environments; kinetic analyses and fitted power-law parameters for toughness and strength recovery; and a video demonstrating autonomous healing of cut elastomers. See DOI: https://doi.org/10.1039/d6lf00078a.

Acknowledgements

This work is dedicated to Christopher K. Ober on the occasion of his retirement, in appreciation of his influential contributions to polymer interfaces and his exemplary role in mentoring generations of scientists. Financial support from the Center for Advanced Materials Processing is gratefully acknowledged. The authors thank Aswin Pitchiya and Ryan Hulchanski for their experimental assistance.

Notes and references

1 Y. Li, Y. Jin, W. Fan and R. Zhou, *J. Leather Sci. Eng.*, 2022, **4**, 24.
2 K. Chang, H. Jia and S.-Y. Gu, *Eur. Polym. J.*, 2019, **112**, 822–831.
3 S. Ghosh, S. Koley, M. Maiti and P. K. Maji, *Chem. – Asian J.*, 2025, **20**, e202401174.
4 S. Kim, H. Jeon, J. M. Koo, D. X. Oh and J. Park, *Adv. Sci.*, 2024, **11**, 2302463.
5 H. Lee, J. Kim, M. Lee and J. Kang, *Chem. Rev.*, 2025, **125**, 11379–11425.
6 A. Rekondo, R. Martin, A. R. de Luzuriaga, G. Cabañero, H. J. Grande and I. Odriozola, *Mater. Horiz.*, 2014, **1**, 237–240.
7 C. J. Kloxin, T. F. Scott, B. J. Adzima and C. N. Bowman, *Macromolecules*, 2010, **43**, 2643–2653.
8 W. Denissen, J. M. Winne and F. E. Du Prez, *Chem. Sci.*, 2016, **7**, 30–38.
9 S. Utrera-Barrios, R. Verdejo, M. A. López-Manchado and M. Hernández Santana, *Mater. Horiz.*, 2020, **7**, 2882–2902.
10 R. Ansaripour, *M.S. Thesis*, Clarkson University, Potsdam, NY, 2019.
11 T. Li, T. Zheng, J. Han, Z. Liu, Z.-X. Guo, Z. Zhuang, J. Xu and B.-H. Guo, *Polymers*, 2019, **11**, 838.
12 H. Ying, Y. Zhang and J. Cheng, *Nat. Commun.*, 2014, **5**, 3218.
13 Z. Wang, S. Gangarapu, J. Escorihuela, G. Fei, H. Zuilhof and H. Xia, *J. Mater. Chem. A*, 2019, **7**, 15933–15943.
14 E. M. Eger and S. Agarwal, *ACS Appl. Polym. Mater.*, 2023, **5**, 5141–5148.
15 I. Omrani, M. S. Zarjani, R. M. Berenjegani and M. R. Nabid, *J. Polym. Environ.*, 2025, **33**, 431–448.
16 X. Zhang, J. Bai, R. Xu, J. Peng, Q. Han, L. He, Y. Ma, G. Da and J. Cui, *ACS Appl. Polym. Mater.*, 2025, **7**, 7025–7034.
17 L. Chen, Z. Dai, W. Lou, P. Jiang, P. Zhang, Y. Bao, X. Gao and J. Xia, *J. Appl. Polym. Sci.*, 2022, **139**, e52694.
18 P. Cordier, F. Tournilhac, C. Soulié-Ziakovic and L. Leibler, *Nature*, 2008, **451**, 977–980.
19 M. W. Urban, D. Davydovich, Y. Yang, T. Demir, Y. Zhang and L. Casabianca, *Science*, 2018, **362**, 220–225.
20 Y. Zhao, R. Yin, H. Wu, Z. Wang, Y. Zhai, K. Kim, C. Do, K. Matyjaszewski and M. R. Bockstaller, *ACS Macro Lett.*, 2023, **12**, 475–480.
21 K. Buaksuntear, P. Limarun, S. Suethao and W. Smitthipong, *Int. J. Mol. Sci.*, 2022, **23**, 6902.
22 Y. Hao, G. Zhu and B. Li, *Ind. Eng. Chem. Res.*, 2024, **63**, 19350–19358.
23 J. M. Winne, L. Leibler and F. E. Du Prez, *Polym. Chem.*, 2019, **10**, 6091–6108.
24 K. Yu, A. Xin and Q. Wang, *J. Mech. Phys. Solids*, 2018, **121**, 409–431.
25 M. Cortes-Clerget, J. Yu, J. R. A. Kincaid, P. Walde, F. Gallou and B. H. Lipshutz, *Chem. Sci.*, 2021, **12**, 4237–4266.
26 G. Li, B. Wang and D. E. Resasco, *ACS Catal.*, 2020, **10**, 1294–1309.
27 B. Afrinaldi, F. Yuliati, H. Judawisastra and L. A. T. W. Asri, *Adv. Polym. Technol.*, 2023, **2023**, 6614326.
28 X. Wan and T. Xu, *Eur. Polym. J.*, 2024, **217**, 113310.
29 H. Huang, Z. Huang, X. Yin, X. Lin, L. Ji, Y. Sun, W. Lin, J. He, J. He and G. Yi, *Ind. Eng. Chem. Res.*, 2025, **64**, 7407–7418.
30 D. Davydovich and M. W. Urban, *Nat. Commun.*, 2020, **11**, 5743.
31 F. Li, H. Qiu, C. Chen, X. Wang, M. Cui, S. Qiu, K. J. Lee, J. Chen, W. B. Ying and J. Zhu, *Macromolecules*, 2025, **58**, 5019–5028.
32 T. Chen, W. Zhang, Y. Li, F. Liu and E.-H. Han, *Appl. Surf. Sci.*, 2024, **667**, 160399.
33 M. Sankarasubramanian, M. Torabizadeh, Z. A. Putnam, J. C. Moosbrugger, M. Y. Huang and S. Krishnan, *Polym. Test.*, 2019, **78**, 105932.
34 L.-Q. Huang, H.-X. Huang, N. Yu, C.-Z. Chen, Y. Liu, G.-H. Hu, J. Du and H. Zhao, *Macromolecules*, 2025, **58**, 1425–1434.
35 A. V. Marenich, C. J. Cramer and D. G. Truhlar, *J. Phys. Chem. B*, 2009, **113**, 6378–6396.
36 K. Fukui, *Acc. Chem. Res.*, 1981, **14**, 363–368.
37 S. Serna, N. S. Purwanto, L. M. Fenimore and J. M. Torkelson, *Polymer*, 2024, **306**, 127232.
38 S. Kozuch and S. Shaik, *Acc. Chem. Res.*, 2011, **44**, 101–110.
39 S. Kozuch, *Wiley Interdiscip. Rev.: Comput. Mol. Sci.*, 2012, **2**, 795–815.

© 2026 The Author(s). Published by the Royal Society of Chemistry

Open Access Article. Published on 27 May 2026. Downloaded on 6/18/2026 4:45:20 AM.
This article is licensed under a Creative Commons Attribution 3.0 Unported Licence.

40 M. J. Suazo and J. M. Torkelson, *ACS Appl. Polym. Mater.*, 2024, **6**, 9209–9218.

41 B. Spitzbarth and R. Eelkema, *Cell Rep. Phys. Sci.*, 2024, **5**, 102010.

42 M. Asgari, A. Abouelmagd and U. Sundararaj, *Appl. Clay Sci.*, 2017, **146**, 439–448.

43 S. Krishnan, A. Klein, M. S. El-Aasser and E. D. Sudol, *Macromolecules*, 2003, **36**, 3511–3518.

44 L. Wu, J. Jasinski and S. Krishnan, *J. Appl. Polym. Sci.*, 2012, **124**, 2154–2170.

45 C. A. Gracia-Fernández, S. Gómez-Barreiro, J. López-Beceiro, J. Tarrío Saavedra, S. Naya and R. Artiaga, *Polym. Test.*, 2010, **29**, 1002–1006.

46 S. G. Musselman, T. M. Santosusso, J. D. Barnes and L. H. Sperling, *J. Polym. Sci., Part B: Polym. Phys.*, 1999, **37**, 2586–2600.

47 H. R. Brown, *Macromolecules*, 2001, **34**, 3720–3724.

48 S. Yadav, N. Misra, Mansi, P. Khanna, M. Jain and L. Khanna, *J. Mol. Model.*, 2023, **29**, 387.

49 H. Kruse, L. Goerigk and S. Grimme, *J. Org. Chem.*, 2012, **77**, 10824–10834.